

JGR Planets

RESEARCH ARTICLE

10.1029/2021JE006858

Key Points:

- Banded structure of Jupiter's microwave brightness is correlated with the cloud-top winds as far down as 100 bars
- Belt/zone contrasts flip sign in the 5–10 bar region, a transition layer coinciding with the water condensation level
- Transition can be explained by stacked meridional circulation cells and/or latitudinal gradients in precipitation

Supporting Information:

Supporting Information may be found in the online version of this article.

Correspondence to:

L. N. Fletcher,
leigh.fletcher@le.ac.uk












Citation:

Fletcher, L. N., Oyafuso, F. A., Allison, M., Ingersoll, A., Li, L., Kaspi, Y., et al. (2021). Jupiter's temperate belt/zone contrasts revealed at depth by Juno microwave observations. *Journal of Geophysical Research: Planets*, 126, e2021JE006858. <https://doi.org/10.1029/2021JE006858>

Received 17 FEB 2021

Accepted 8 JUL 2021

Jupiter's Temperate Belt/Zone Contrasts Revealed at Depth by Juno Microwave Observations

L. N. Fletcher¹ , F. A. Oyafuso², M. Allison³ , A. Ingersoll⁴ , L. Li⁵ , Y. Kaspi⁶ , E. Galanti⁶ , M. H. Wong⁷, G. S. Orton² , K. Duer⁶, Z. Zhang⁴ , C. Li⁸, T. Guillot⁹ , S. M. Levin² , and S. Bolton¹⁰ 

¹School of Physics and Astronomy, University of Leicester, Leicester, UK, ²Jet Propulsion Laboratory, California Institute of Technology, Pasadena, CA, USA, ³Goddard Institute for Space Studies, New York, NY, USA, ⁴California Institute of Technology, Pasadena, CA, USA, ⁵University of Houston, Houston, TX, USA, ⁶Department of Earth and Planetary Sciences, Weizmann Institute of Science, Rehovot, Israel, ⁷SETI Institute, Mountain View, CA, USA, ⁸University of Michigan, Ann Arbor, MI, USA, ⁹Université Côte d'Azur, OCA, Lagrange CNRS, Nice, France, ¹⁰Southwest Research Institute, San Antonio, TX, USA

Abstract Juno microwave radiometer (MWR) observations of Jupiter's midlatitudes reveal a strong correlation between brightness temperature contrasts and zonal winds, confirming that the banded structure extends throughout the troposphere. However, the microwave brightness gradient is observed to change sign with depth: the belts are microwave-bright in the $p < 5$ bar range and microwave-dark in the $p > 10$ bar range. The transition level (which we call the “jovicline”) is evident in the MWR 11.5 cm channel, which samples the 5–14 bar range when using the limb-darkening at all emission angles. The transition is located between 4 and 10 bars, and implies that belts change with depth from being NH_3 -depleted to NH_3 -enriched, or from physically warm to physically cool, or more likely a combination of both. The change in character occurs near the statically stable layer associated with water condensation. The implications of the transition are discussed in terms of ammonia redistribution via meridional circulation cells with opposing flows above and below the water condensation layer, and in terms of the “mushball” precipitation model, which predicts steeper vertical ammonia gradients in the belts versus the zones. We show via the moist thermal wind equation that both the temperature and ammonia interpretations can lead to vertical shear on the zonal winds, but the shear is $\sim 50 \times$ weaker if only NH_3 gradients are considered. Conversely, if MWR observations are associated with kinetic temperature gradients then it would produce zonal winds that increase in strength down to the “jovicline”, consistent with Galileo probe measurements; then decay slowly at higher pressures.

Plain Language Summary One of the core scientific questions for NASA's Juno mission was to explore how Jupiter's famous banded structure might change below the top-most clouds. Did the alternating bands of temperatures, winds, composition, and clouds simply represent the top of a much deeper circulation pattern? Juno's microwave radiometer is capable of peering through the clouds to reveal structures extending to great depths, and has revealed a surprise: belts and zones do persist to pressures of 100 bars or more, but they flip their character at a level which we call the “jovicline,” coinciding with the depths at which water clouds are expected to form and generate a stable layer. This transition from microwave-bright belts (ammonia depleted and/or physically warm) in the upper layers, to microwave-dark belts (ammonia enriched or physically cool) in the deeper layers, and vice versa for the zones, may have implications for the shear on the Jupiter's zonal winds, indicating winds that strengthen with depth down to the jovicline, before decaying slowly at higher pressures. The origins of the transition is explored in terms of meridional circulations that change with depth, and in terms of models where strong precipitation dominates in the belts.

1. Introduction

The colorful bands of Jupiter have been the planet's defining characteristic for centuries, discovered mere decades after the invention of the telescope (Hockey, 1999). The tropospheric bands are organized by east-west zonal jets (e.g., Porco et al., 2003; Read et al., 2006), which separate regions exhibiting different temperatures (Pirraglia et al., 1981), different gaseous composition (e.g., ammonia and phosphine, Fletcher

et al., 2009; Gierasch et al., 1986), and different aerosol properties (the reflectivity and color of the clouds and hazes, e.g., West et al., 2004). These bands were historically characterized as high-albedo zones and low-albedo belts, but we adopt a belt-zone nomenclature based on their vorticity. The zones are anticyclonic and the belts are cyclonic. Zones are cool in the upper troposphere (i.e., adiabatic expansion above the clouds and below the stably stratified tropopause) and have eastward (prograde) jets on their poleward edges, generating potential vorticity gradients that act as barriers to meridional mixing (Read et al., 2006). Conversely, belts are warm (adiabatic compression) and feature westward (retrograde) jets on their poleward boundaries.

The upper-tropospheric belt/zone temperature contrasts encourage condensation of volatiles (e.g., ammonia) in cooler regions, typically producing reflective aerosols in zones and cloud-free conditions in belts, although the correspondence between the zonal jets and the opacity of the clouds (sensed at 5 μm , Antuñaño et al., 2019) only really holds at low latitudes. Conversely, the correspondence between the observed cloud-tracked winds and upper tropospheric temperatures persists up to high latitudes near $\pm 60^\circ$ (Conrath & Pirraglia, 1983; Flasar, 1986; Fletcher et al., 2016; Simon-Miller et al., 2006) and implies, via the thermal wind equation (Holton, 2004), that the zonal jets decay with altitude from the cloud-tops to the tropopause (Conrath et al., 1990; Pirraglia et al., 1981). The source of the dissipative mechanism causing this decay with height remains unclear and has never been directly observed, but could be related to wave or eddy stresses opposing the winds (Orsolini & Leovy, 1993; Pirraglia, 1989). Finally, the latitudinal distribution of chemicals such as ammonia (Achterberg et al., 2006; de Pater et al., 2016; Gierasch et al., 1986; C. Li, Ingersoll, et al., 2017), phosphine (Fletcher et al., 2009; Giles et al., 2017; Grassi et al., 2020), and para-hydrogen (Conrath et al., 1998; Fletcher, de Pater, et al., 2017), combined with the observed temperature and aerosol distributions, suggest that the atmospheric circulation in the upper troposphere is dominated by rising motions over zones, zone-to-belt meridional transport at high altitude, and sinking over the belts. This is the “classical” picture of belt/zone circulation envisaged by Hess and Panofsky (1951) and Stone (1976), and is often likened to “Hadley-like” circulations in the terrestrial atmosphere, whereby warm tropical air rises and moves poleward (a thermally direct circulation), being deflected eastward by the Coriolis effect to generate sub-tropical jet streams.

Insights from Voyager, Galileo, and Cassini have challenged this conceptual picture, as reviewed by Fletcher et al. (2020). Lightning was detected as optical flashes (Baines et al., 2007; Gierasch et al., 2000; Little et al., 1999), and was found to be prevalent in the belts but either absent or obscured in the zones. This suggested moist air converging and rising in the belts, potentially in narrow convective plumes embedded within regions of net subsidence (Ingersoll et al., 2000; Lunine & Hunten, 1987; Showman & de Pater, 2005). Furthermore, cloud-tracking by Voyager (Ingersoll et al., 1981) and Cassini (Salyk et al., 2006) identified eddies converging and supplying momentum to the eastward jets, via a process analogous to Earth’s Ferrel cells (Vallis, 2006). This forcing of the jets by flux convergence can be confined to shallow layers within the clouds and yet still produce jets that extend deep (Lian & Showman, 2008). However, the forcing must be balanced by a compensating meridional flow, which has rising motions in belts, belt-to-zone meridional transport, and sinking over the zones. Such a belt/zone circulation is opposite to that postulated for the upper troposphere, and has led to a hypothesis of “stacked circulation cells,” with deep Ferrel-like cells dominated by eddy-forcing of the zonal winds, and upper cells of eddy-dissipation and wind decay (Fletcher et al., 2020; Ingersoll et al., 2000; Showman & de Pater, 2005), with a poorly defined transition somewhere within the “weather layer” above the water clouds. Such counter-rotating stacked cells have been observed in numerical simulations with prescribed heating and eddy momentum fluxes (Yamazaki et al., 2005; Zuchowski et al., 2009), and general circulation models (GCMs) hint at changes to the magnitude of eddy-momentum flux convergence as a function of altitude (Spiga et al., 2020; Young et al., 2018).

Juno’s exploration of Jupiter provides an opportunity to explore belt/zone contrasts below the cloud tops, and to test the stacked-cell hypothesis. Jupiter’s winds have been found to extend to $\sim 3,000$ km below the clouds (Guillot et al., 2018; Kaspi et al., 2018), to the level where Ohmic dissipation may become important (Cao & Stevenson, 2017; Galanti & Kaspi, 2021; Kaspi et al., 2020; Liu et al., 2008). The slow decay with depth suggests that the meridional temperature gradients must be weak but opposite to that seen in the upper troposphere (where winds strengthen with depth). Observations by Juno’s microwave radiometer (MWR) found the vertical distribution of ammonia to be variable across latitudes from 40°S to 40°N ,

with widespread depletion down to 40–60 bar (perijove 1, August 27, 2016, Bolton et al., 2017; Ingersoll et al., 2017; C. Li, Ingersoll, et al., 2017). Previously, the ammonia cross section was observed to be dominated by an NH_3 -rich column at the equator, flanked by NH_3 -depleted belts evident in both the mid-IR (Achterberg et al., 2006; Fletcher et al., 2016) and ground-based millimeter and sub-millimeter observations (de Pater et al., 2016). Although some form of NH_3 depletion might result from precipitation (Ingersoll et al., 2017), it was a challenge to get this below the 10-bar level (C. Li & Chen, 2019) without invoking a process using robust “mushballs” (Guillot, Stevenson, et al., 2020) composed of mixed-phase ammonia/water condensates (Weidenschilling & Lewis, 1973). From these Juno microwave observations in 2016, Ingersoll et al. (2017) noted that the correlation of ammonia variations with the belts and zones was rather weak at $p < 2$ bars, but that the correlation was better from $p = 40$ to 60 bars, where the belts have higher ammonia abundances than the zones, opposite to what was seen in the upper troposphere. The very existence of localized NH_3 anomalies suggests that upwelling and subsidence must be occurring in the presence of a vertical NH_3 gradient throughout the range of MWR sensitivity. Furthermore, Duer et al. (2020) used these same PJ1 data to reveal correlations between cloud-top winds and the NH_3 abundances and concentration gradients, supporting the inference of meridional circulation cells in the altitude range sounded by MWR. Finally, observations from the Very Large Array (VLA) in 2014 (probing as deep as ~ 7 bar at 10 cm, de Pater, Sault, Wong, et al., 2019) also tentatively suggested a brightness temperature reversal for a single band near the 21°N jet, but this was for a single location and a shallower pressure than the phenomenon identified in our study.

In this study, we investigate the correlation between Jupiter's cloud-top winds and microwave brightness using observations spanning the first 2 years of Juno operations (2016–2018), focusing on the midlatitude temperate domains away from the strong NH_3 gradients at the equator (Section 2). We report the existence of a level at which the microwave brightness contrasts reverse, which we call the “jovicline” via analogy to terrestrial oceanography. By exploiting the emission-angle dependence of the brightness temperatures to sound a range of altitudes, we show in Section 3 how we constrain the pressure of the transition between microwave-bright belts in the upper troposphere, and microwave-dark belts in the deeper atmosphere. We aim to show, in a model-independent way, that the transition is evident from the data alone, irrespective of its interpretation. Section 4 shows how the identification of this transition relates to atmospheric temperatures, winds, and ammonia within the stacked-cell hypothesis, and explores alternative scenarios for the observed contrasts.

2. Juno Microwave Contrasts

2.1. MWR Observations

In this section, we demonstrate the correlation between microwave brightness temperature gradients and the locations of Jupiter's cloud-tracked zonal jets. The MWR (Janssen et al., 2017) is part of a suite of remote sensing instruments on the Juno spacecraft (Bolton et al., 2017), which has been in a 53-day polar orbit around Jupiter since July 2016. The elliptical orbits bring the spinning spacecraft within 3,000–4,000 km of the jovian cloud tops during the ~ 2 -hour pole-to-pole perijove (PJ) passes, during which time the fields-of-view of the six MWR receivers (spanning 0.6–21.9 GHz, or 1.4–50 cm) are swept over the scene. MWR measurements provide two key capabilities over previous ground-based radio measurements: (a) they are able to unambiguously separate Jupiter's synchrotron emission from atmospheric thermal emission, particularly important for observations at $p > 5$ bars, and (b) the 2-rpm spin of the spacecraft allows a direct measurement of brightness as a function of emission angle for each position, which will be key to this study of the belt/zone transition.

Oyafuso et al. (2020) describe how the jovian brightness temperatures, T_B , are deconvolved from the antenna temperatures, removing the galactic and synchrotron backgrounds and accounting for the antenna beam pattern and contributions from sidelobes (a feature of the beam pattern). The result is a T_B as if it were measured along a narrow pencil-beam targeting a particular latitude ϕ (sampled on a grid of 255 points from pole to pole) and emission angle. The dependence of the brightness on the emission-angle cosine μ is known as the limb darkening, and is expressed via the quadratic function (Oyafuso et al., 2020):

$$T_B(\mu) = \xi(\mu) \left[c_0 - c_1 \frac{1 - \mu}{1 - \mu^*} + \frac{c_2 (\mu - \mu^*)(1 - \mu)}{2(1 - \mu^*)^2} \right] \quad (1)$$

where μ^* is set to 0.8; the coefficient c_0 is the nadir brightness temperature ($\mu = 1.0$), c_1 is the absolute limb darkening when $\mu = \mu^* = 0.8$ (chosen to correspond to an emission angle of 37°), and c_2 represents a further decline in brightness at 53° ($\mu = 0.6$) beyond that obtained from a linear extrapolation from nadir to 37° . The range of μ between 1.0 and 0.6 was selected as the most appropriate for the MWR emission angle coverage. The parameter $\xi(\mu)$ is a shape function that accounts for imperfections in the quadratic fit to the limb-darkening dependence beyond 53° (see Oyafuso et al., 2020, for full details).

This work uses $T_B(\phi, \mu)$ reconstructed from the fitted coefficients in Equation 1 for each latitude from PJ1 (August 27, 2016) through PJ12 (April 1, 2018). Data from PJ10 (December 2017) and PJ11 (February 2018) were not used because the spacecraft orientation was optimized for gravity science (i.e., favoring continuous Earth pointing), and no data were obtained during PJ2 (October 2016). MWR samples narrow longitudinal swaths during each of the nine selected perijoves, which are used to represent Jupiter's zonally averaged microwave brightness. However, to filter out coefficients that resulted from poor quality quadratic fits to the observed limb darkening, we construct a weighted average of each coefficient at each latitude, weighting by (a) a local χ^2 describing the goodness-of-fit of the quadratic in Equation 1 to the $T_B(\phi, \mu)$ measurements, and by (b) a spatial contribution function that weights by the square root of the effective number of measurements at a given latitude (see Oyafuso et al., 2020, for details).

The weighted-average $T_B(\phi, \mu)$ is shown in Figure 1 for each of the six channels, revealing a banded structure at all pressure levels sampled by these data, from ~ 120 bars at 50 cm (Channel 1) to ~ 0.6 bars at 1.4 cm (Channel 6). The percentage limb darkening at 45° emission angle ranges from 1% at 0.6 bars (i.e., minimal limb darkening) to 13%–15% at 100 bars (strong limb darkening), consistent with Oyafuso et al. (2020). No attempt is made in Figure 1 to adjust for the poleward increase in brightness resulting from the change in Jupiter's atmospheric scale height, which depends on effective gravitational acceleration (see Section 2.2). The tropical contrasts between the microwave-dark equatorial zone (EZ, 6°N – 6°S) and the microwave-bright North/South Equatorial Belts (NEB $6.0 - 15.2^\circ\text{N}$ and SEB $6.0 - 17.4^\circ\text{S}$) dominate Figure 1 at all pressure levels, interpreted by C. Li, Ingersoll, et al. (2017) and Ingersoll et al. (2017) as a column of enriched NH_3 gas at the equator, with strong NH_3 depletion over the neighboring belts. For our purposes, these strong tropical contrasts dominate the color scale in Figure 1 and render the midlatitude belt/zone contrasts harder to see, so we show the nadir T_B polewards of $\pm 20^\circ$ latitude (i.e., the c_0 coefficients of Equation 1) in Figure 2, to be discussed in the next section.

2.2. Nadir Brightness Gradients

Figure 2 demonstrates how the filtering process of Oyafuso et al. (2020) identifies measurements that appear to differ substantially from other perijoves. For example, the microwave-bright southern periphery of the Great Red Spot was observed on PJ7 (C. Li, Oyafuso, et al., 2017) and is a significant outlier near 25°S , but the poor goodness-of-fit (χ^2) for the quadratic in Equation 1 for these latitudes means that PJ7 does not contribute significantly to our average. Similarly, a screening algorithm is used to remove observations contaminated by synchrotron emission, meaning that there will be fewer measurements available in affected latitudes for the quadratic fitting (see Section 2.5 of Oyafuso et al., 2020). This was particularly true for PJ3 and PJ4 at northern midlatitudes, which appear anomalously bright but are constrained by very few uncontaminated measurements, such that their reduced weighting via the spatial contribution function minimizes their contribution to the weighted average. The thick black line shows our best estimate of the microwave banding (consistent with Oyafuso et al., 2020), and is compared to the locations of the eastward (prograde, dashed) and westward (retrograde, dotted) jets as determined by Cassini/ISS cloud-tracking of zonal winds u (Porco et al., 2003), extracted via identifying locations where the vorticity $-\partial u / \partial y = 0$ (where y is the north-south distance in kilometers, accounting for the radius of curvature for an oblate spheroid). Similar calculations using Hubble cloud-tracked winds in 2017–2019 are shown in the supporting information, but the location of the jets has not changed significantly with time (Tollefson et al., 2017; Wong et al., 2020). We

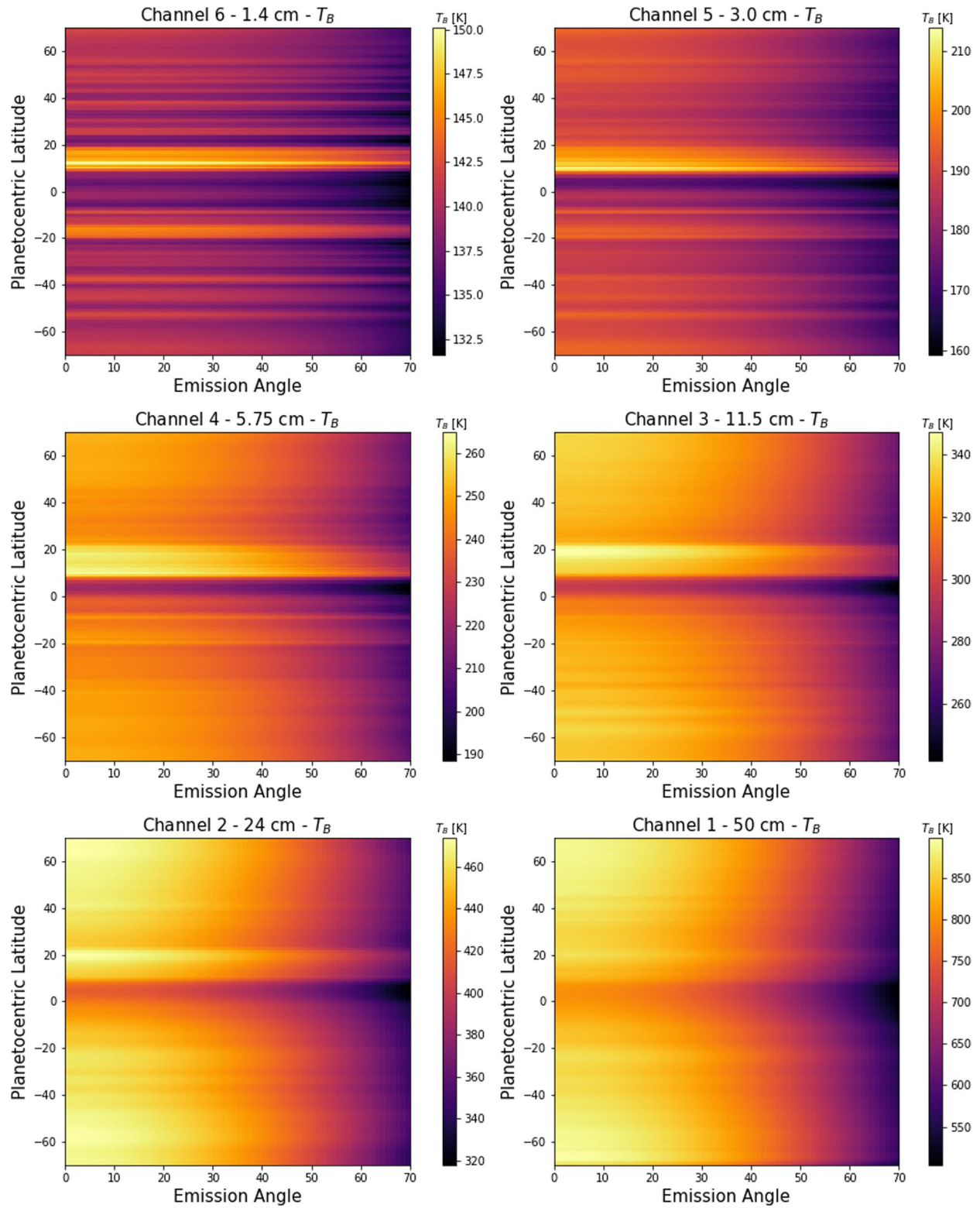


Figure 1. Deconvolved brightness temperatures as a function of emission angle and planetocentric latitude, formed from a weighted average of nine Juno perijoves between August 2016 and April 2018. Banded structure is observed in all channels, but the contrast is dominated by the tropics. No attempt has been made to remove the latitudinal dependence of T_B on atmospheric scale height (which depends on effective gravitational acceleration), see Section 2.2.

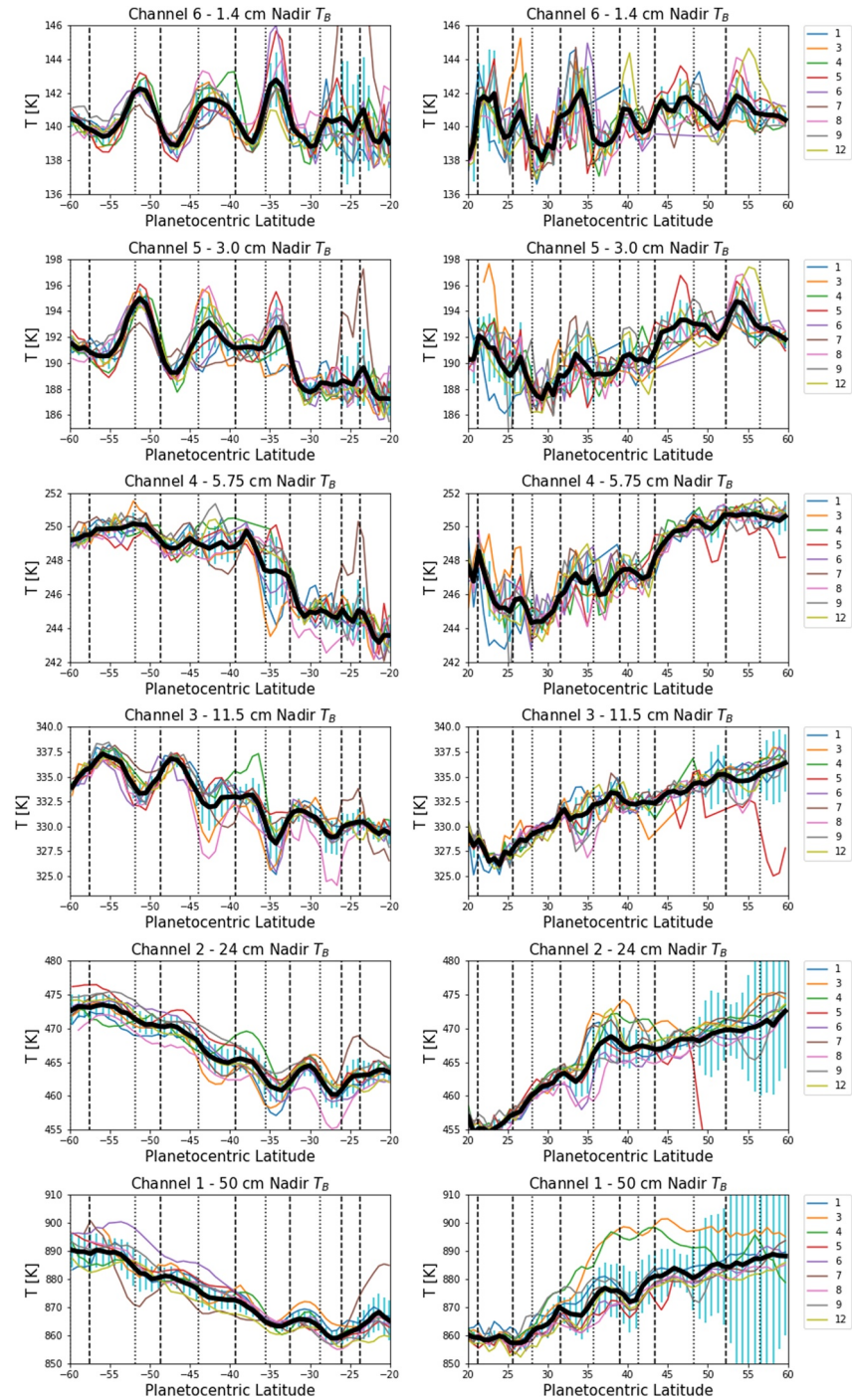


Figure 2. Nadir microwave brightness temperatures for all nine perijoves (colored lines) compared to the weighted average (thick black line) to show the filtering process. Uncertainties on the weighted average are shown by the blue bars, indicating discrepancies between perijoves. These are compared to the peaks of eastward (dashed) and westward (dotted) zonal winds as measured by Cassini (Porco et al., 2003). Note that uncertainties become large at high northern latitudes for wavelengths longer than 11.5 cm, due to the introduction of synchrotron noise into the beam.

use these velocity minima and maxima to define the locations of Jupiter's cloud-top belts and zones, rather than the aerosol opacity, color, and reflectivity, which are not good proxies for the underlying zonal wind structure (Fletcher et al., 2020).

To better emphasize the gradients observed by MWR, we convert the T_B measurements into a “pseudo-shear” Δ by analogy to the thermal wind equation (Holton, 2004), assuming *constant pressure surfaces*:

$$\Delta = -\frac{g}{fT_B} \frac{\partial T_B}{\partial y} \quad (2)$$

where we replace the kinetic temperature of the atmosphere with the brightness temperature. f is the Coriolis parameter, g is the gravitational acceleration at the particular pressure and latitude, and the brightness temperature derivative is evaluated on isobars (constant-pressure surfaces). At this stage, we make no connection between Δ and the shear on the zonal jets, but use this formalism simply to denote the edges of the microwave belts and zones. We plot Δ in Figure 3, showing how the peaks in the microwave brightness gradients are co-located with the cloud-tracked zonal jets (the strength of the correlation will be explored below). Dashed lines are eastward jets (zones on the equatorward sides, belts on the poleward sides); dotted lines are westward jets (zones on the poleward side, belts on the equatorward side). Blue points are used to denote a negative gradient, red points are used for a positive gradient, and the patterns provide our first sign that a transition in belt/zone gradients occurs between the deep-sensing channels 1–3 (6 to greater than 100 bars), and the shallow-sensing channels 4–6 (0.6–5.0 bars).

We can see this reversal in Δ by tracking single jets in Figure 3. For example, the prograde jets at 48.6° S and 32.5°S coincide with local minima of negative Δ in the 0.6–5.0 bar range, but flip to being local maxima of positive Δ in the 10–100 bar range. Conversely, the retrograde jets at 35.5°S and 43.9°S coincide with local maxima of positive Δ at shallow depths, and local minima of negative Δ at deeper levels. This reversal in Δ has the effect of transitioning a traditional jovian belt (with prograde jets on their equatorward edges) from microwave-bright at shallow levels to microwave-dark at deeper levels, and vice versa for zones (with prograde jets on their poleward edges), as previously identified in PJ1 observations between 40°S and 40°N by Ingersoll et al. (2017). The correspondence between Δ and the cloud-tracked winds is not perfect, and we explore the statistical significance of the correlations in Section 2.3. In particular, we caution that (a) the correspondence is clear in the south but only suggestive (at best) in the north, and (b) a residual equator-to-pole gradient remains in the data as a shift toward negative values of Δ in the deep-sounding channels 1–3. The origin of this deep poleward gradient of deep temperature and/or NH_3 , superimposed onto the banded structure, is the topic of an ongoing investigation.

We omitted latitudes smaller than $\pm 20^\circ$ from Figures 2 and 3. However, the Δ reversal is prominent for the retrograde NEBn and SEBs jets at 15.2°N and 17.4°S, respectively (from positive Δ at shallow depths, to negative Δ at deeper levels). This can be seen in Figure 1, where an extremely bright band is observed in deep-sensing Channels 1–3 in the 15.2 – 21.3°N region (the North Tropical Zone), but not in shallow-sensing Channels 4–6. Right at the equator, the prograde jets bounding the EZ (the NEBs at 6.0°N and the SEBn at 6.0°S) are the only jets where no Δ reversal is observed, it remains negative at all levels given that the equatorial zone is always microwave-dark in Figure 1. This is consistent with the EZ being an unusual region of elevated NH_3 abundance (C. Li, Ingersoll, et al., 2017), and what follows focuses on the banded structure away from the equatorial belts and zones.

Finally, the Cassini/ISS winds (shown later in Figure 10) show the existence of small notches in the $\partial u / \partial y$ profiles near 26.1°S and 25.6°N. We have treated these as additional eastward jets in Figure 3, although this is not standard nomenclature (they exist in the middle of the NTB and STB, respectively). The STB wind feature appears to be strong adjacent to the “structured sectors” known as the STB Ghost, Spectre, and other dark segments (Iñurrigarro et al., 2020), and absent elsewhere (J. Rogers, *pers.comms.*). The NTB feature could be sub-dividing the belt in two. However, MWR reveals that there are substantial brightness gradients (Δ , with a reversal in sign) associated with both of these features in each channel, suggesting that they are more important to the flow field than suggested by the cloud-tracked winds. These additional “mid-temperature-belt” jets will be the subject of future investigations.

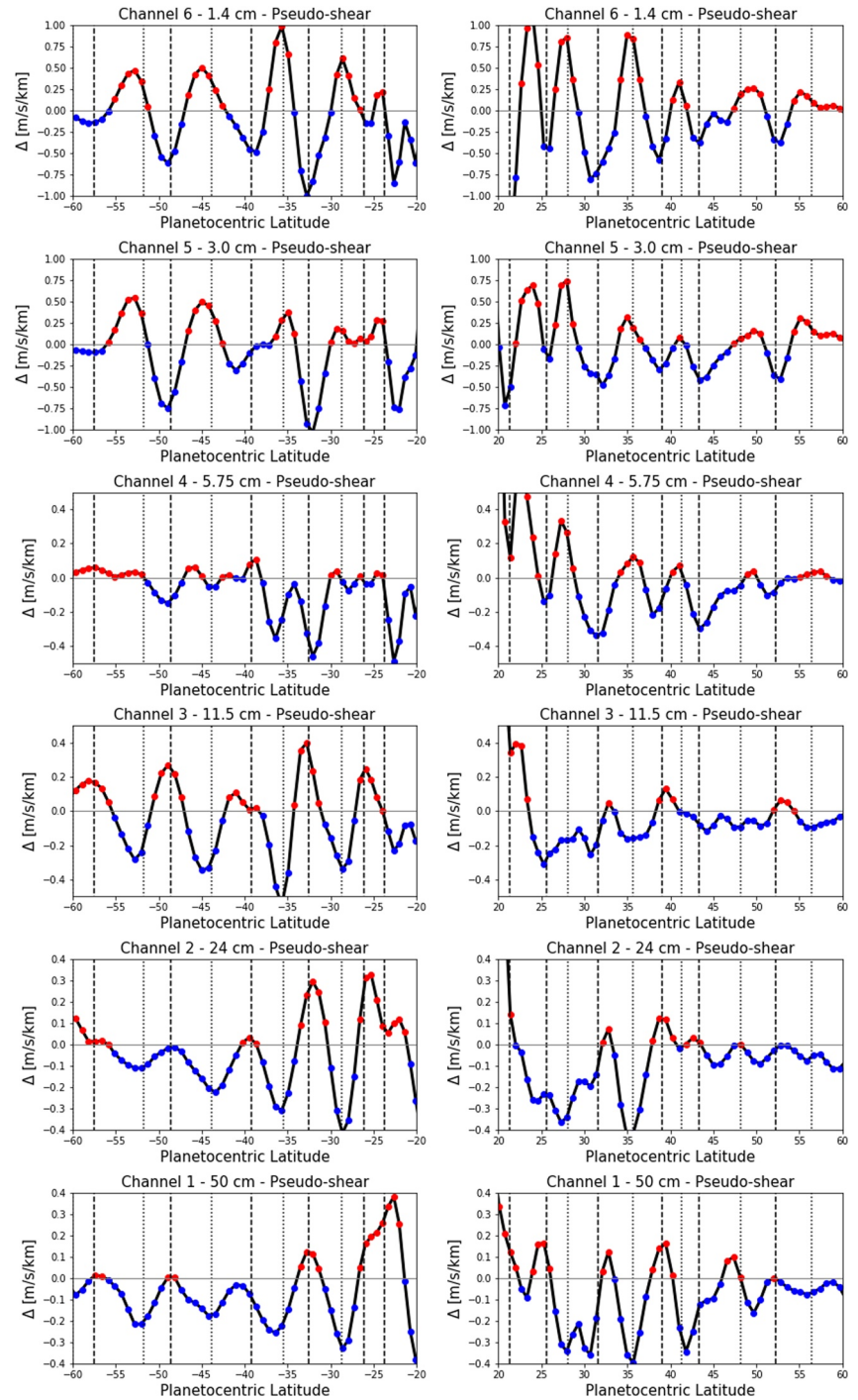


Figure 3. Nadir microwave brightness gradients for temperate latitudes, corrected by both the Coriolis parameter and gravitational acceleration to represent “pseudo-shear” in m/s/km. Regions of negative pseudo-shear are represented by blue points, regions of positive pseudo-shear are represented by red points. These are compared to the peaks of eastward (dashed) and westward (dotted) zonal winds as measured by Cassini (Porco et al., 2003).

2.3. Correlation Analysis

In Section 2.2, we noted that the correlations between the cloud-top winds and the microwave brightness gradients, Δ , were not perfect. Figure 4 provides a scatter plot of the nadir Δ versus the Cassini/ISS cloud-top

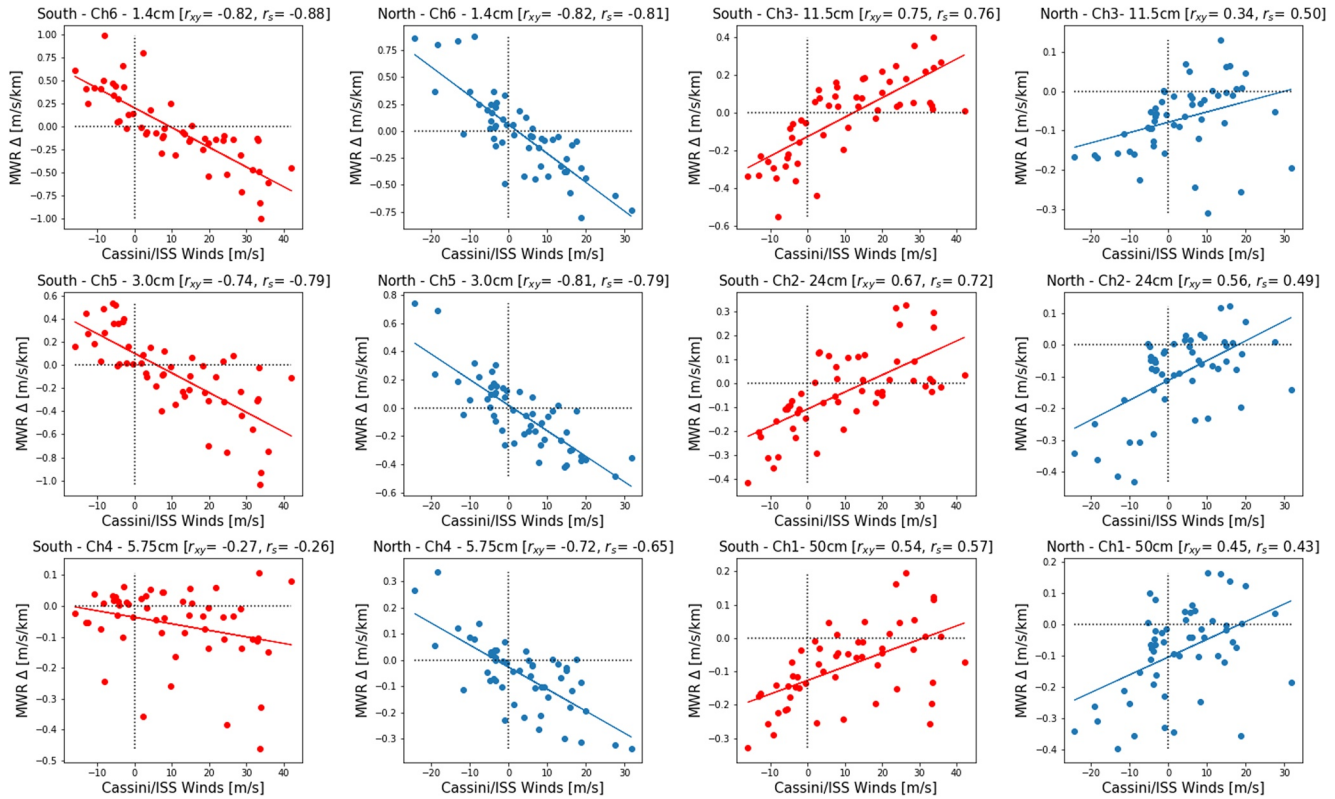


Figure 4. Scatter plots revealing negative (channels 4–6, left columns) and positive (channels 1–3, right columns) correlations between the nadir microwave T_B gradients Δ and the Cassini cloud-tracked winds. Only latitudes between 25° and 65° in each hemisphere are included. Southern-hemisphere correlations are in red, northern-hemisphere correlations are in blue. A linear trend line has been added as a guide. The Pearson r_{xy} and Spearman's ranked r_s correlation coefficients are provided for each channel and hemisphere. See Figures S1 and S2 for similar scatter plots computed using Hubble winds in 2017–2019 (Tollefson et al., 2017; Wong et al., 2020).

winds for the northern ($25 - 65^\circ\text{N}$) and southern ($25 - 65^\circ\text{S}$) hemispheres, for all six channels. We restrict this analysis to temperate midlatitudes $> \pm 25^\circ$, excluding Jupiter's fastest retrograde jet (the SEBs at 17.4°S) and the fastest prograde jet (the NTBs at 21.3°N) as their extreme speeds would otherwise dominate the correlation analysis, and discuss the importance of these asymmetric jets later in Section 3.3.2. As expected from the comparison of Δ with the jet peaks in Figure 3, the scatter plots fall into two groups: deep-sounding channels (1–3, 11.5–50 cm sounding 10–100 bars) with a positive correlation between prograde velocities and Δ , and shallow-sounding channels (4–6, 1.4–5.75 cm, sounding 0.6–5.0 bars) with negative correlation between prograde velocities and Δ .

Figure 4 shows qualitatively that (a) channel 4 (5.75 cm) shows the weakest correlation in the south, but channel 3 (11.5 cm) shows the weakest correlation in the north, and (b) the correlations look generally stronger in the south than the north. To quantify this, we compute the Pearson correlation coefficient (r_{xy} , measuring the linear correlation between the winds and Δ) and the Spearman rank correlation coefficient (r_s , assessing the strength of the link between the two parameters), and record them in Figure 4. We also compute the probability values (p -values) for each correlation, with values significantly smaller than 0.05 allowing us to firmly reject the null hypothesis that the winds and Δ are uncorrelated (these are provided in the supporting information, Tables S1 and S2). Confirming the qualitative assessment in Figure 4, p -values are smallest (and the correlation is highly statistically significant) for channel 5–6, and highest but still significant (~ 0.01) for channel 4. We also computed these correlations using Hubble-derived zonal wind fields in 2017 (Tollefson et al., 2017) and 2019 (Wong et al., 2020), finding small improvements to the correlation without changing the conclusions—these computations can be found in our Text S1.

The strength of the correlation depends on which perijoves are included in our weighted average, and which latitudes we include in the figure. In our Text S2, we test the robustness of the correlations by selecting

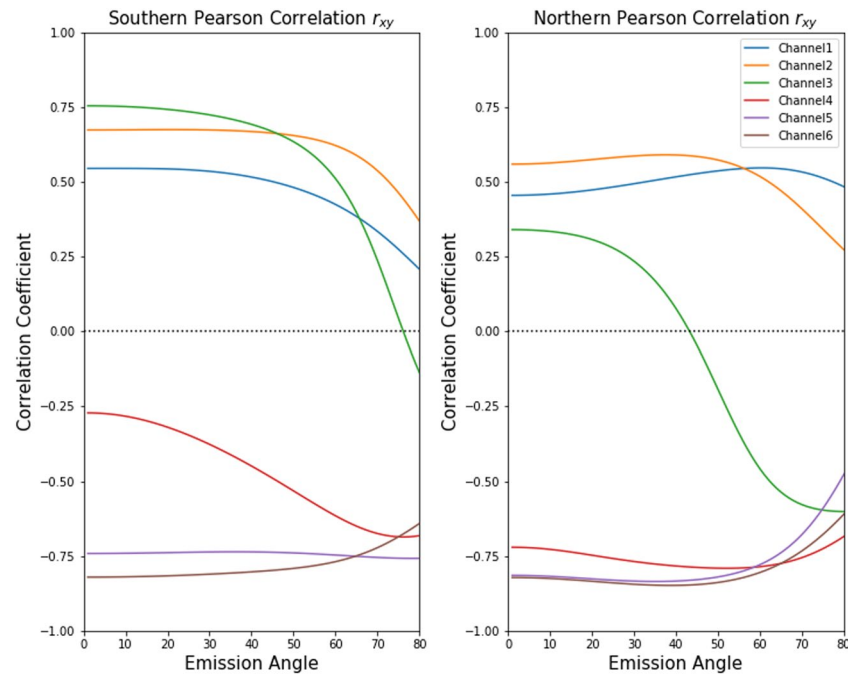


Figure 5. Linear correlation between microwave T_B gradients (Δ_μ) and cloud-top winds calculated on a 1° grid at all emission angles (see Section 2.3 for a discussion of reliability at emission angles exceeding $\sim 60^\circ$). The channels naturally fall into two groups (positive and negative correlations), with a crossover in Channel 3. These coefficients are hemispheric averages over the $25 - 65^\circ$ latitude ranges.

random pairs of perijoves from the nine studied here, recomputing the correlation coefficients and p -values for each pair and showing that the correlation remains significant, as it was when it was first noted in PJ1 data (August 2016) (Ingersoll et al., 2017; Oyafuso et al., 2020)—Figures S4–S6. We also recomputed the correlation coefficients assuming winds that varied along cylinders parallel to the rotation axis (Duer et al., 2020), and found negligible changes to the strength of the correlations observed in Figure 4.

Finally, we can extend the nadir-only analysis of Figure 4 to all emission angles sampled by MWR, and represented by the limb-darkened brightness temperatures in Figure 1. We now calculate Δ_μ for all $T_B(\phi, \mu)$ values (the μ subscript denotes that we now include all emission angles), and recompute the Pearson r_{xy} in Figure 5. The six channels still naturally fall into two groups—negative correlation at shallow depths, positive correlation at deeper levels. But Figure 5 also shows that the transition from positive to negative correlation occurs within a single channel, channel 3 (11.5 cm), near 45° emission angle in the north, and 75° emission angle in the south, although we stress that these are averages over all the jets in the $25 - 65^\circ$ latitude ranges in both hemispheres. As contribution functions shift higher with increasing emission angle, this provides a rough estimate of the transition pressure as being somewhere between the 14-bar level sounded in channel 3 and the 5-bar level sounded by channel 4. However, we caution that the deconvolution process of Oyafuso et al. (2020) avoided contributions from emission angles exceeding 53° , such that the southern hemisphere 75° crossover in channel 3 depends somewhat on our choice of functional form to represent the limb darkening (Equation 1). This should be considered at the edge of the MWR capabilities (i.e., the crossover happens somewhere between the depths sensed by channels 3 and 4), whereas the northern hemisphere crossover in channel 3 is more convincing. Indeed, the channel-3 switch from weak positive correlation at nadir ($r_{xy} = 0.34$, $p_{xy} = 1 \times 10^{-2}$) to slightly stronger negative correlation at 60° emission angle ($r_{xy} = -0.46$, $p_{xy} = 5 \times 10^{-4}$) in Figure 5 is statistically significant. Figure S3 of the supporting information shows how these p_{xy} values vary with emission angle. In Section 3, we use the limb-darkening dependence to refine the altitude of the transition point.

3. Assessing the Transition Depth

The MWR data presented in the previous section demonstrated the existence of a transition in the sign of the microwave T_B brightness gradients (Δ), somewhere within the 5–14-bar region sounded by Channels 4 and 3. This could be seen directly from the deconvolved MWR observations, using the limb-darkening coefficients extracted using the techniques in Oyafuso et al. (2020). The identification of this transition is independent of any radiative transfer modeling for emission angles smaller than 53° . However, the shape function in Equation 1 (estimated from the discrepancy between modeled limb-darkening and the simple polynomial fits, Oyafuso et al., 2020) begins to deviate from unity beyond 53° , introducing some weak model dependence to the deconvolved MWR observations at the highest angles. Further constraints on the altitude of the transition requires an estimation of the angular dependence of MWR contribution functions at each wavelength. We will use the contribution functions to assign each measured T_B to an estimated pressure level.

3.1. MWR Contribution Functions

We use the *Jupiter Atmospheric Radiative Transfer Model* (JAMRT, Janssen et al., 2017) to calculate the dependence of the contribution function on emission angle, as shown in Figure 6. Instead of using the standard JAMRT model with a lower boundary condition of 351 ppm of NH_3 (equivalent to $2.76 \times$ protosolar ammonia, C. Li et al., 2020), and an NH_3 profile declining with height due to equilibrium cloud condensation (see Text S3 and Figure S7), we instead use the retrieved NH_3 distribution on a 5° latitude grid averaged over PJ1 through PJ9, as presented by Guillot, Li, et al. (2020) using the same techniques as C. Li, Ingersoll, et al. (2017). In order to fit the higher-than-expected microwave brightnesses measured by Juno (Bolton et al., 2017), these retrievals required NH_3 depletion compared to the standard JAMRT model, so our computed contribution functions generally probe higher pressures than those reported elsewhere in the literature (Janssen et al., 2017). We assume a moist adiabat for the thermal structure based on NH_3 , H_2S and H_2O , and all other atmospheric species and boundary conditions are as described in Oyafuso et al. (2020).

The left-hand column of Figure 6 shows how the MWR channels probe higher altitudes with increasing emission angle, and how the contribution functions are relatively broad in the vertical direction. The central column reveals how the latitudinal dependence derived by Guillot, Li, et al. (2020) influences the nadir contribution. Because of the enhanced NH_3 retrieved in the Equatorial Zone, MWR channels tend to probe slightly higher in the equatorial region than they do in the neighboring equatorial belts and the temperate midlatitudes. For the right column of Figure 6, we identify the pressure at the peak of the contribution function for each emission angle for six scenarios: three spatially averaged regions (northern midlatitudes 20°N – 40°N , the equator 5°N – 5°S , and southern midlatitudes 20°S – 40°S) and two different models of NH_3 opacity—those of Hanley et al. (2009) and Bellotti et al. (2016). As we are primarily concerned with midlatitudes in this study, we average the midlatitude contribution functions for both opacity models and both hemispheres, and employ a quadratic spline fit to interpolate over the emission angles in our experiments. This provides smoothly varying functions for the angular dependence of the contribution functions at midlatitudes, based on realistic NH_3 abundances.

The calculations in Figure 6 reveal that, between emission angles of 0° and 70° , MWR sounds a range of pressures in each channel: 1.4 cm (channel 6, 0.55–0.64 bar), 3.0 cm (channel 5, 0.8–1.6 bar), 5.75 cm (channel 4, 2.3–4.8 bar), 11.5 cm (channel 3, 6.0–13.8 bar), 24 cm (channel 2, 17.7–34.4 bar) and 50 cm (channel 1, 44–117 bar). As expected, we find substantially less altitude sensitivity at the shortest wavelengths (channels 5 and 6, sounding $p < 2$ bar) compared to the highest wavelengths (channels 1 and 2, sounding $p > 20$ bar). This is consistent with the extent of the limb darkening shown in Figure 1. We stress that the contribution functions remain extremely model dependent, varying with the retrieved ammonia abundances and assumptions about the lapse rate. Furthermore, the peaks represent broad functions, with extensions to lower and higher pressures, particularly at the longest wavelengths (Janssen et al., 2017). Channel 1 (50 cm) also displays significant sensitivity to pressures approaching 1,000 bars, but this remains questionable given uncertainties about ammonia and water opacity at these long wavelengths (C. Li et al., 2020).

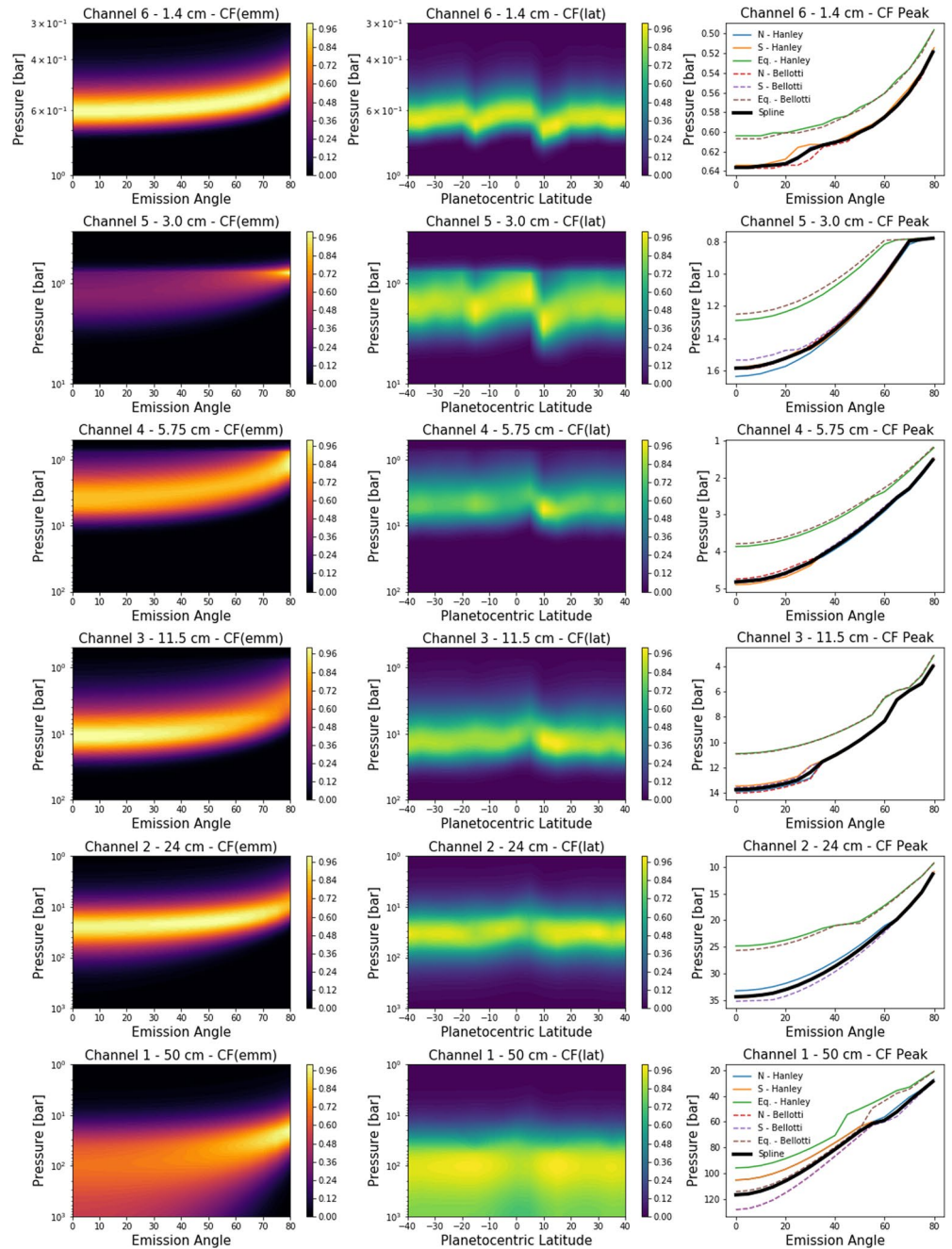


Figure 6. Contribution functions based on the retrieved distribution of NH_3 versus latitude and pressure based on Guillot, Li, et al. (2020), with a modified NH_3 gradient at $p < 0.6$ bars to remove a discontinuity. Left: Normalized contribution functions as a function of emission angle for the equator. Centre: Normalized contribution functions at zero emission angle (nadir view) for all latitudes. Right: Peak pressure of the contribution function averaged over three regions (north 20°N to 40°N; south 20°S to 40°S, and equator 5°N to 5°S) using two different NH_3 opacity models—Hanley et al. (2009) as the solid lines and Bellotti et al. (2016) as the dashed lines. The solid black line is the spline-interpolated contribution function described in the main text.

Based on the contribution functions in Figure 6, we can approximate the depth of the Δ_μ transition from Figure 5, where the flip from positive to negative correlations is observed in Channel 3 (11.5 cm). In the northern temperate domain this occurs near $\theta = 40 - 50^\circ$ (Figure 5), placing the transition near 10–11 bars. Similarly, the southern transition was at $\theta = 70 - 80^\circ$, implying a transition nearer 4–6 bars. These are averaged over all temperature latitudes in each hemisphere, and will be further refined below.

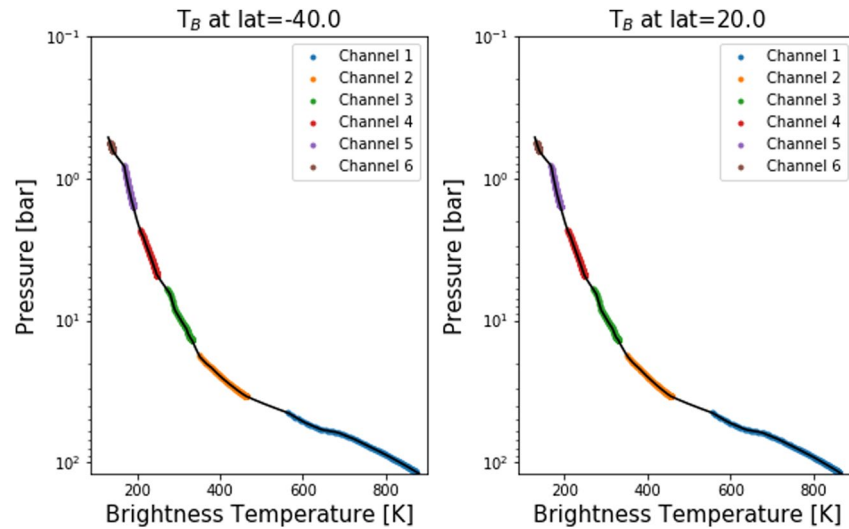


Figure 7. Vertical profiles of T_B at two different latitudes, estimated by assigning limb-darkened microwave radiometer (MWR) measurements to discrete pressure levels using the contribution function peaks in Figure 6. The y-axis indicates the pressure of the contribution peak at different emission angles, and different colors indicate different channels, with a smooth interpolation over regions without MWR sensitivity (retaining emission angles smaller than 70°). Note that this is not from a spectral inversion, therefore does not represent kinetic temperatures—it is simply a reprojection of the MWR measurements.

3.2. Constructing a 2D Brightness Temperature Cross Section

We now use the emission-angle dependence of the MWR contribution functions (Figure 6) to assign the model-independent $T_B(\phi, \mu)$ measurements from Figure 1 to a vertical pressure grid. We stress that this is a method for reprojecting the T_B measurements onto a pressure grid using a model-dependent contribution function, and should not be confused with a full inversion of the measurements to derive real kinetic temperatures. This reprojection greatly expands the vertical sensitivity compared with the nadir-only approach, but we encounter substantial challenges, as shown in two example $T_B(p)$ profiles in Figure 7. First, the vertical sensitivity of adjacent MWR channels do not overlap with one another for emission angles smaller than 70° , so we are required to interpolate between them. Second, adjacent channels do not line up sufficiently to produce a completely smooth vertical structure, resulting in some kinks in the $T_B(p)$ profiles. This is particularly true for the transition between channels 5 and 6, where there is an offset of tens of degrees. This is likely due to the assumptions underpinning the contribution function calculations: even though we have used realistic NH_3 distributions, differences in the NH_3 abundance could shift the peak sensitivity up and down and possibly allow better alignment of the channels. Third, we are effectively treating the contribution function as a delta function, assigning the T_B to a unique pressure level and ignoring the broad range of pressures sounded in Figure 6—this will be particularly problematic for channel 1, which has a broad contribution function reaching pressures of 1,000 bars or greater. And finally, the $T_B(\phi, \mu)$ has some dependence on the chosen functional form for the limb darkening (Equation 1) for high emission angles ($\mu < 0.6$).

We construct $T_B(p)$ profiles for all latitudes and assemble them into a $T_B(\phi, p)$ cross section in Figure 8, compared to the locations of the cloud-top zonal winds. Although this has the appearance of a kinetic temperature cross section common in atmospheric physics, we caution that these T_B values are the product of both temperature and opacity variations. As for the nadir T_B profiles in Figure 2, the gradients away from the tropics are rather subtle, so we compute the “pseudo-shear” Δ_μ for every pressure level in Figure 9a. Here, the transition from $\Delta_\mu > 0$ (red) to $\Delta_\mu < 0$ (blue), or vice versa, is visible throughout the temperate midlatitudes (as well as the retrograde jets on the poleward edges of the NEB and SEB, discussed in Section 2.2).

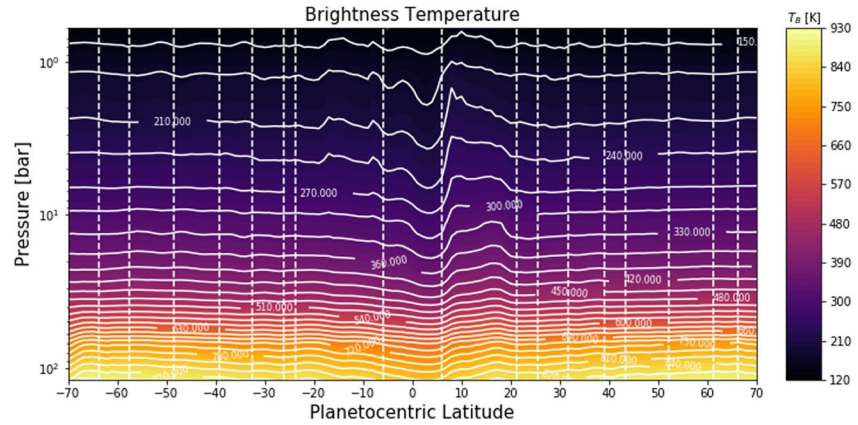


Figure 8. 2D cross section of microwave radiometer (MWR) brightness temperature $T_B(\phi, p)$, reprojected by assigning limb-darkened T_B measurements to discrete pressure levels using the angular dependence of the contribution functions from Figure 6. Vertical dashed lines indicate the locations of the cloud-top prograde jets.

The transition occurs where $\Delta_\mu = 0$ and is evidently latitude-dependent, so we plot Δ_μ for individual eastward and westward jets in Figures 9b and 9c, highlighting the high degree of variability from jet to jet. The vertical trends in Δ_μ are clearest for the broad westward jets, where Figure 9c confirms that shears are generally positive for $p < 10$ bars and negative for $p > 10$ bars, although there is significant variability across the latitudes. However, for the eastward jets the picture is unclear—these are generally (but not always) experiencing negative Δ_μ for $p < 10$ bars, and they have small values ($\Delta_\mu < \pm 0.25$ m/s/km) for $p > 10$ bars, sometimes positive, sometimes negative. We show in Section 3.3 that this weak Δ_μ , if interpreted as real kinetic temperature contrasts, might imply that eastward jets largely remain eastward at all depths to 100 bars, whereas the westward jets with larger Δ_μ variations can change direction with depth. The lack of clarity in Δ_μ at the prograde jet locations could be a spatial-resolution effect related to their narrow or “sharp” latitudinal widths, compared to the broad retrograde jets. Figure 9 suggests that the transition typically occurs in the 5–10 bar range, and is certainly easier to see in the locations of the westward jets. In the next section, we explore what these pseudo-shears might imply about the zonal winds.

3.3. Zonal Wind Interpretation

3.3.1. Dry Thermal Wind Balance

Prior to this point, we have been careful to describe the microwave brightness contrasts in terms of a pseudo-shear, Δ , because both opacity variations (mainly NH_3) and kinetic temperature variations (T) could be responsible for gradients in T_B . We now consider the extreme case where our measured Δ_μ is assumed to be the true vertical windshear (i.e., that $T_B = T$, and that all brightness variations are considered to be due to kinetic temperature), and employ the “dry” thermal wind equation (Holton, 2004), neglecting contributions from molecular weight gradients (see Section 3.3.4):

$$\frac{\partial u}{\partial z} \approx -\frac{g}{fT} \left(\frac{\partial T}{\partial y} \right)_p \quad (3)$$

Here y is the north-south distance in kilometers, and the temperature gradients are measured on constant-pressure surfaces. We estimate the gravitational acceleration $g(p, \phi)$ using the combined gravitational and centrifugal potential of Buccino et al. (2020), reproducing their effective gravity at 1 bar. We then use the ideal gas law to estimate the height $z(p, \phi)$, which reproduces the altitudes recorded by the Galileo probe (Seiff et al., 1998). Both grids are provided with our supporting information in Figure S8.

We use Equation 3 to integrate the cloud-top winds (Porco et al., 2003) as a function of depth. This quantity, the “pseudo-wind,” is shown as a cross section in Figure 10b and for the individual jet locations in Figures 10c and 10d. For simplicity, we integrate along the local vertical, rather than along cylinders parallel to the rotation axis, meaning that we cannot estimate winds close to the equator where the Coriolis

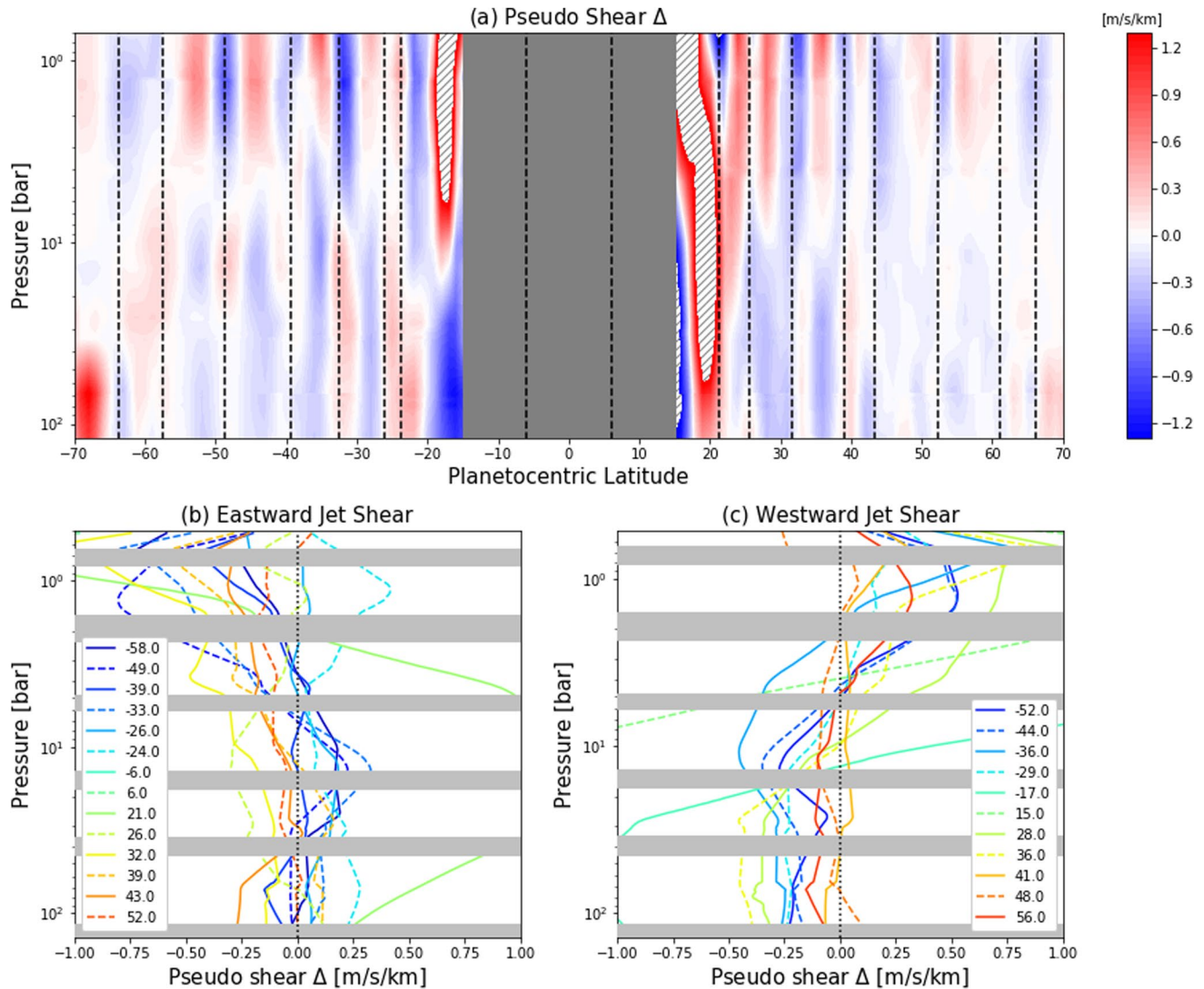


Figure 9. (a) 2D cross section of microwave radiometer (MWR) brightness gradient $\Delta_\mu(\phi, p)$, or pseudo shear, in units of m/s/km, constructed from the $T_B(\phi, p)$ cross section in Figure 8. The color scale is saturated at ± 1.3 m/s/km to emphasise gradients at midlatitudes, values of Δ_μ exceeding this range are shown as gray hatches. Tropical regions at latitudes less than 15° are omitted. Vertical dashed lines indicate the locations of the cloud-top prograde jets. (b and c) Extracting the MWR pseudoshear Δ_μ from (a) near to the locations of the eastward (b) and westward (c) jets, as shown by the planetocentric latitudes in the legends. Gray horizontal bars indicate regions without MWR vertical sensitivity (as defined by Figure 6) and discontinuities in the calculation of Δ_μ . Tropical pseudoshears exceed ± 1 m/s/km over much of the domain, so cannot be seen on this figure. The pseudoshear generally reverses sign near the 10-bar level, especially for southern-hemisphere jets.

parameter tends to zero. However, as we are dealing here with a relatively shallow layer of atmosphere, with a small aspect ratio between the vertical and horizontal scales, this form of thermal wind is sufficient (Kaspi et al., 2009). The latitude and depth-dependence of the gravity field is taken into account.

For the midlatitudes, Figure 10 reveals the consequence of having a windshear that changes sign in the 5–14 bar region: winds will increase with depth below the top-most clouds to reach an extremum in the 5–14 bar range, then the sense of the shear reverses to cause a decay with increasing depth. For the prograde jets, the windshear is sufficiently weak that the jets mostly remain eastward throughout the domain sensed by MWR (i.e., $p < 100$ bars)—most temperate jets at 100 bar would be in the 10–75 m/s range, not dissimilar from the speeds of those eastward jets at 1 bar. The pseudo-shear is stronger for the retrograde jets, suggesting that the direction of the temperate jets could even switch from retrograde to prograde at pressures exceeding 20–30 bars (Figure 10d). In most cases, the magnitude of these jets at 100 bars remains small (< 25

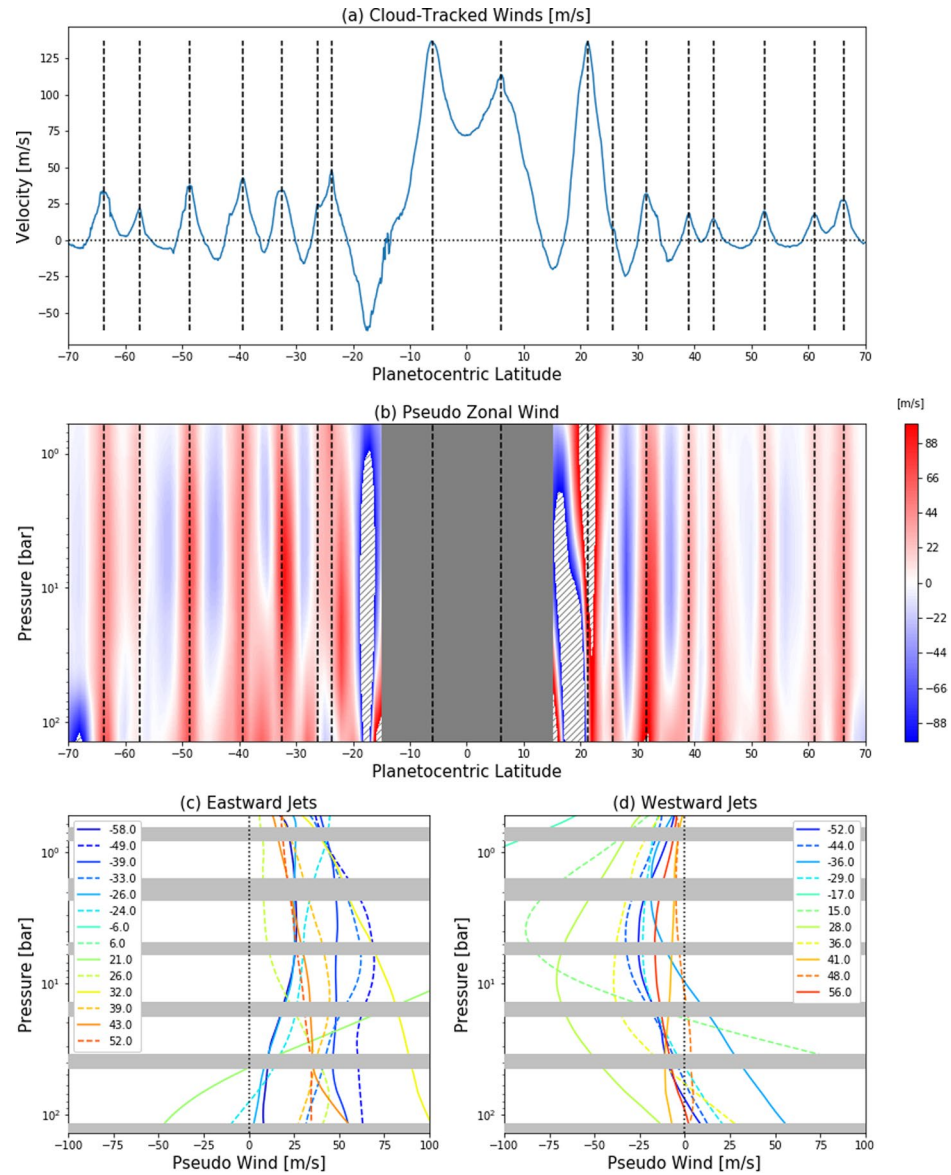


Figure 10. Calculated pseudo winds (b) assuming that Δ_{μ} can be equated to the vertical shear on the zonal winds (i.e., that $T = T_B$). Integration is along the local vertical, rather than along cylinders parallel to the rotation axis. Cloud-tracked winds from Cassini (Porco et al., 2003) are shown in panel (a) for comparison. Speeds exceeding 100 m/s have been omitted (gray hatches), and speeds peak where Δ_{μ} changes sign. Vertical dashed lines indicate the locations of the cloud-top prograde jets. Low latitudes near the equator are omitted as the Coriolis parameter tends to zero (it varies as the sine of the latitude) and Δ_{μ} therefore tends to infinity. The lower panels show the microwave radiometer (MWR) pseudowinds from (b), extracted near to the locations of the eastward (c) and westward (d) jets, as shown by the planetocentric latitudes in the legends. Gray horizontal bars indicate regions without MWR vertical sensitivity (as defined by Figure 6) and discontinuities in the calculation of Δ_{μ} . Tropical windspeeds calculated in this manner exceed ± 100 m/s over much of the domain, so cannot be seen on this figure. Note that this figure implies strengthening winds at $p > 100$ bar, whereas Juno gravity measurements require that they must ultimately begin to decay at higher pressures (Kaspi et al., 2018).

m/s), although some of the jets approach 100 m/s at 100 bar, which is inconsistent with constraints imposed by the gravity measurements (Galanti et al., 2021). This suggests that we cannot consider the T_B variations in the deepest MWR channels to be solely driven by kinetic temperatures, and NH_3 (and potentially H_2O) must play a role. Furthermore, we caution that the contribution functions for the MWR channels are highly model dependent, meaning that different assumptions about ammonia and water opacity could affect how

the pseudo-shear Δ_μ is distributed with height. We also stress that integration of the windshear is prone to magnification of small errors with increasing depths, such that these deep winds should be treated with suspicion even if the assumption of $T_B = T$ were appropriate.

3.3.2. Comparison to Juno Gravity

It is natural to ask whether the inferred pseudo-winds are consistent with the results of Juno's gravity measurements (Guillot et al., 2018; Kaspi et al., 2018), which suggest a variety of potential wind profiles decaying to the 3,000-km level, depending on the sensitivity to the measured odd gravity harmonics J_3 , J_5 , J_7 and J_9 (Duer et al., 2020). An increase in the temperate winds to the transition point at 5–14 bar, followed by a weak decay of the winds to higher pressures, is broadly consistent with the need for some form of decay profile in the interior (Kaspi et al., 2018, 2020). The gravity measurements are not directly sensitive to the winds at the altitudes sensed by MWR, but the analysis of the gravity data must assume a vertical profile for the velocity, which happens to be well matched to the cloud-top winds (Kaspi et al., 2018). Indeed, Duer et al. (2020) found that interior wind profiles that diverged from those measured at the cloud tops (i.e., depth-dependent flow profiles) could also be consistent with the gravity data, but concluded that they were statistically unlikely.

The primary asymmetry in Jupiter's zonal winds is between the fastest retrograde jet in the south (the SEBs at 17.4°S) and the fastest prograde jet in the north (the NTBs at 21.3°N). Figure 10b implies that this low-latitude asymmetry weakens with depth, suggesting our kinetic-temperature-only assumption (i.e., that $T_B = T$), and the implied strong shears on the equatorial jets in the $p > 10$ bar region of Figure 10c, are not realistic. Conversely, provided this low-latitude asymmetry is maintained, then the gravity measurements display a limited sensitivity to what the jets are doing at midlatitudes poleward of $\pm 25^\circ$, in terms of both direction and magnitude. By retaining the observed cloud-top low-latitude winds within the 25°S to 25°N range, and introducing random velocity profiles for the temperate jets at higher latitudes, Galanti et al. (2021) showed that this change has a limited effect on the goodness-of-fit to the odd gravity harmonics, as well as the even harmonics J_6 , J_8 , and J_{10} (their Section 4 and Figure 4). In essence, a modification of the midlatitude zonal jets below the clouds is not ruled out by the gravity data, provided that their magnitude remains small, which is the case in Figure 10 with our extreme assumption that Δ_μ represents the true vertical windshear. Nevertheless, an optimal match to the gravity data still requires that the wind profile in the range 50°S to 50°N is unchanged from those measured at the cloud tops (Galanti et al., 2021). It is more likely that both T and NH_3 control the microwave brightness, such that the true vertical windshear is smaller than presented in Figure 9, making it more consistent with the Juno gravity results.

3.3.3. Comparison to Galileo Probe

We can also compare the inferred structure of the pseudo winds from MWR to the only in situ measurement of winds by the Galileo probe in 1995 (Atkinson et al., 1998). The comparison is made complicated because (a) the probe descended into an anomalous tropospheric feature called a “5- μm hot spot” which may have influenced the measured winds, and (b) this region was at the boundary between the EZ and NEB where the strongest Δ is measured (related to the equatorial NH_3 enhancement, C. Li, Ingersoll, et al., 2017). Nevertheless, the wind profile was found to approximately double from the 1-bar level to ~ 5 bars, then level off and potentially show a weak decay with increasing pressure. This was supported by Cassini cloud-tracking (L. Li, Ingersoll, Vasavada, Simon-Miller, Achterberg, et al., 2006), which suggested that the NEBs jet at 6°N strengthened with depth from the 0.5-bar level to the ~ 5 bar level by more than 90 m/s, and also by an investigation of the stability of the zonal jets (Dowling, 1995), as discussed in Section 3.3.5. A decay of the zonal winds for $p < 1$ bar is also supported by thermal-infrared observations (e.g., Fletcher et al., 2016; Pirraglia et al., 1981; Simon-Miller et al., 2006), suggesting that this shear region may actually extend from 0.5 to 5.0 bars.

By taking gradients of the results from Galileo's Doppler Wind Experiment (Atkinson et al., 1998), we find that this is consistent with having negative vertical windshear for $p < 5$ bars (~ -2 m/s/km at 2 bars), and weakly positive windshear for $p > 5$ bars (~ 0.25 m/s/km at 10 bars). The uncertainties on the Galileo wind profile start to grow large for $p > 15$ bar, implying that both positive, zero, or negative windshears are possible (Atkinson, 2001). Specifically for the NEB, this is inconsistent with the Δ measured by MWR (which

remains negative throughout the 1–100 bar domain, presumably as a result of strong NH_3 contrasts such that the $T = T_B$ assumption is invalid here). However, the Galileo-measured equatorial windshears are comparable in magnitude to the Δ in Figure 9 for midlatitudes, suggesting that temperate jets that increase in strength down to the transition point, and then decay slowly with depth at higher pressures, are consistent with the structure observed by the Galileo probe, whether or not that measurement was truly representative of the equatorial zonal winds.

Finally, Galanti et al. (2021) explore whether Juno gravity measurements can still be reproduced if the zonal winds truly experience this doubling in strength from the cloud level to the 5-bar level, finding that plausible solutions can still be found, only with the winds decaying with a more baroclinic vertical profile compared to the Kaspi et al. (2018) profile in the upper 2,000 km, below which the winds decay more slowly, reaching 10% of their original value at 3,000 km. This different wind decay could be considered as a viable alternative to the decay profiles in Kaspi et al. (2018), but additional constraints on the wind profiles in the 1–10 bar range are sorely needed, as discussed in Section 3.3.5.

3.3.4. Moist Thermal Wind Balance

In this section, we describe how latitudinal gradients in molecular weight can still lead to vertical wind-shear, even if the kinetic temperature remains uniform. In the case where both compositional and thermal variations result in latitudinal density gradients *along constant-pressure surfaces*, we express the geostrophic thermal wind equation (Holton, 2004) in its less familiar “moist” or “virtual” form (sometimes known as a “humidity wind” equation, Sun et al., 1991) in altitude coordinates z :

$$\frac{fT}{g} \frac{\partial u}{\partial z} = - \left(\frac{\partial T_v}{\partial y} \right)_p \quad (4)$$

where symbols have the same meanings as in Section 3.3.1. Sun et al. (1991) demonstrated that compositional gradients could have a significant influence on the windshear in hydrogen-rich atmospheres, most important with the observed enrichments of Uranus and Neptune over solar composition, but here we explore the implications for Jupiter's troposphere. The virtual temperature T_v is defined as:

$$T_v = \frac{T}{1 + \Sigma \alpha_c q_c} \quad (5)$$

Here q_c is the mole fraction, α_c is a coefficient for each constituent equal to $(\mu_c / \mu_d) - 1$, the ratio of the molecular weight of the constituent (μ_c) to the molecular weight of dry air (μ_d). The Σ symbol implies a sum over the relevant gases (NH_3 , H_2S , H_2O). We do not directly relate T_v to the observed T_B gradients, but introduce it simply to account for the effects of molecular weight gradients on vertical shears. The derivation below differs from Equation 7 of Sun et al. (1991) because we use mole fractions, whereas they used mass mixing ratios. In the case where these constituents are considered to be variable, we adjust the thermal wind equation to become:

$$\frac{fT}{g} \frac{\partial u}{\partial z} = - \frac{\partial}{\partial y} \left(\frac{T}{1 + \Sigma \alpha_c q_c} \right) \quad (6)$$

$$= - \frac{1}{1 + \Sigma \alpha_c q_c} \left(\frac{\partial T}{\partial y} - \frac{T}{1 + \Sigma \alpha_c q_c} \frac{\partial}{\partial y} (\Sigma \alpha_c q_c) \right) \quad (7)$$

If we retain the molecular weight contributions of all three condensables, but assume that both H_2S and H_2O are latitudinally uniform to remove their derivatives, then we can rewrite the T_v gradient considering only contributions from the temperature and NH_3 gradients:

$$\frac{fT}{g} \frac{\partial u}{\partial z} = - \frac{1}{1 + \Sigma \alpha_c q_c} \left(\frac{\partial T}{\partial y} - \frac{T \alpha_{\text{NH}_3}}{1 + \Sigma \alpha_c q_c} \frac{\partial q_{\text{NH}_3}}{\partial y} \right) \quad (8)$$

In the case where we assume no latitudinal ammonia gradients, and with $\Sigma \alpha_c q_c \ll 1$ (a reasonable assumption in the upper troposphere where mole fractions of each species are $< 10^{-3}$, but more questionable at depth), this simplifies to the familiar dry thermal wind equation in Equation 3, as discussed in Section 3.3.1. However, if we assume negligible latitudinal contrasts in temperature, following previous MWR analyses

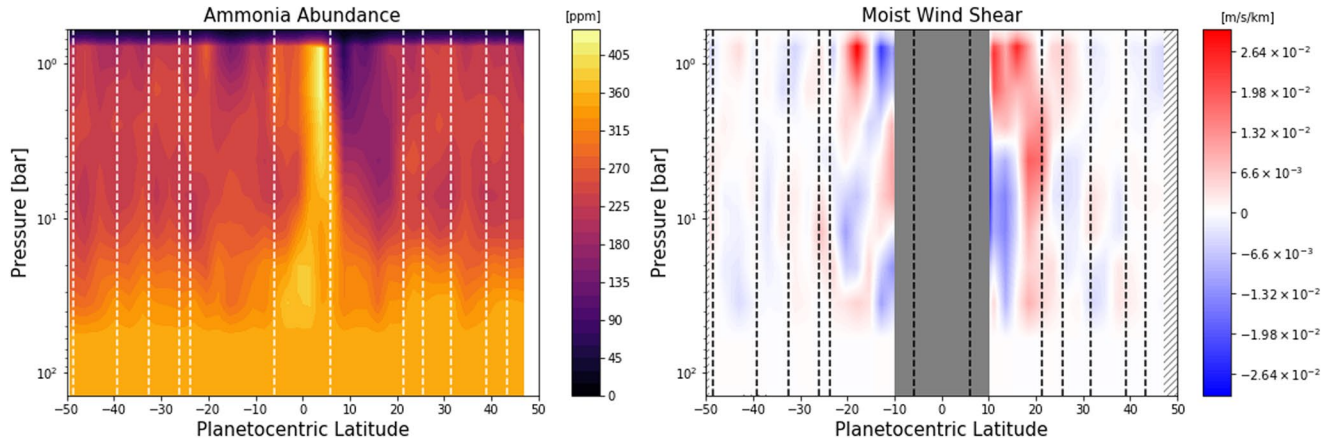


Figure 11. Zonal-mean cross section of ammonia derived by Guillot, Li, et al. (2020) based on the technique of C. Li, Ingersoll, et al. (2017). The gradients are used to estimate the moist shear based on NH_3 alone, which is some $50 \times$ smaller than that in Figure 9 for midlatitudes.

(Ingersoll et al., 2017; C. Li, Ingersoll, et al., 2017), and again assuming $\Sigma \alpha_c q_c \ll 1$, then we find that ammonia gradients can still result in vertical windshear:

$$\frac{\partial u}{\partial z} \approx + \frac{g \alpha_{\text{NH}_3}}{f} \frac{\partial q_{\text{NH}_3}}{\partial y} \quad (9)$$

Here $\alpha_{\text{NH}_3} = (\mu_{\text{NH}_3} / \mu_d) - 1 = 6.36$, with $\mu_{\text{NH}_3} = 17.031$ g/mol and the dry molecular weight of jovian air is $\mu_d \approx 2.313$ g/mol, assuming 86.26% H_2 , 13.54% He, and 0.20% CH_4 (von Zahn et al., 1998; Wong et al., 2004). Note the change in sign between the two forms of the wind equation (Equations 3 and 9), and how it relates to the MWR brightness temperature observations. Local maxima in microwave brightness over belts in the upper troposphere ($p < 5$ bar) would still be in balance with negative $\partial u / \partial z$ (i.e., wind decay with height) irrespective of whether this is due to an *increased* temperature or an NH_3 minimum. Local minima in T_B in the deeper troposphere ($p > 10$ bar) would still be in balance with positive $\partial u / \partial z$ (i.e., wind decay with depth), irrespective of whether this is due to an *decreased* temperature or an NH_3 maximum. In both the temperature-only and the ammonia-only cases, the vertical windshear would have the same sign. But how significant is this effect?

Guillot, Li, et al. (2020) provide a retrieved latitude cross section of NH_3 abundances averaged over PJ1 to PJ9 which we can use to measure $\partial q_{\text{NH}_3} / \partial y$ as an estimate of $\partial u / \partial z$ (Figure 11). Although the resolution of their inversion is lower than the resolution of the MWR brightness temperature used in this study, Figure 11 confirms the flip in sign of the shear as a function of depth, and shows that the peaks in the shear remain co-located with the locations of Jupiter's cloud-top jets. Note that this NH_3 cross section was the basis for our contribution function calculation in Figure 6.

Based on NH_3 alone, the shear is strongest near the equator, approaching -0.25 m/s/km for the NEBs jet (not shown) in the 0.6–2.0 bar region, which is $\sim 10\%$ of the shear needed to explain those measured by the Galileo probe. In the temperate midlatitudes, we find $\partial q_{\text{NH}_3} / \partial y$ in the range $\pm 1.5 \times 10^{-8} \text{ km}^{-1}$, which equates to windshears in the range ± 0.03 m/s/km, at least $50 \times$ smaller than the brightness-temperature derived Δ_μ in Figure 9a. On this basis, if NH_3 contrasts are the only significant contributor to MWR brightness gradients, then the integrated midlatitude winds will be largely barotropic in the 1–100 bar range.

As a final thought experiment, we extended Equation 9 to include the influence of H_2O , still assuming that $\Sigma(\alpha_c q_c) \ll 1$:

$$\frac{\partial u}{\partial z} \approx + \frac{g}{f} \left(\alpha_{\text{NH}_3} \frac{\partial q_{\text{NH}_3}}{\partial y} + \alpha_{\text{H}_2\text{O}} \frac{\partial q_{\text{H}_2\text{O}}}{\partial y} \right) \quad (10)$$

Here $\alpha_{\text{H}_2\text{O}} = (\mu_{\text{H}_2\text{O}} / \mu_d) - 1 = 6.78$, with $\mu_{\text{H}_2\text{O}} = 18.015$ g/mol. The latitudinal distribution of H_2O is currently unknown, so we estimate $\partial q_{\text{H}_2\text{O}} / \partial y$ by scaling the equatorial water profile of C. Li et al. (2020) using the latitude dependence of the NH_3 results in Figure 11. This is a very crude assumption, but supposes

that the same processes shaping the NH_3 distribution (Ferrel cells or precipitation, see Section 4) are also governing the as-yet-unmeasured H_2O distribution (Guillot, Li, et al., 2020). The contribution of water to moist thermal wind balance is $\sim 3 \times$ larger than that of ammonia—at midlatitudes, in the 5–50 bar region, this would produce shears of ± 0.1 m/s/km (a factor of ~ 10 smaller than those shown at midlatitudes in Figure 9), rising to -1 m/s/km for the NEBs jet, which is too large (and too negative) to be consistent with the windshear directly measured by the Galileo Probe for $p > 5$ bar, potentially suggesting that such strong water contrasts are unlikely in the equatorial domain.

The effect of such a weak moist windshear at midlatitudes would be that the winds would be almost barotropic over the domain sounded by MWR (1–100 bars), which would also be consistent with the Juno gravity measurements (Galanti et al., 2021). However, it is counter to that shown from the dry windshear equation in Figure 10, and counter to the Galileo probe wind measurements that showed strong variability with depth. There remains much debate over whether the winds observed by Galileo (Atkinson et al., 1998; L. Li, Ingersoll, Vasavada, Simon-Miller, Del Genio, et al., 2006) were a local consequence of the Rossby-wave dynamics of the $5\text{-}\mu\text{m}$ hot spot (Showman & Dowling, 2000), or globally representative of the shear on the NEBs jet. If the latter is true, then the Galileo winds suggest the need for some kinetic temperature contrasts (i.e., dry windshear) in at least the 0.5–5.0 bar region sounded by MWR channels 4–6, because the moist windshears discussed above are insufficient. However, without being able to uniquely separate ammonia and kinetic temperatures in a microwave inversion, MWR conclusions about zonal winds still range from nearly *vertically uniform* to *vertically variable* with a transition near 5–14 bars, and it might even be possible that the dry and moist windshears actually oppose one another at some locations (i.e., a region that is both warm and enriched in volatiles). Additional constraints on deep kinetic temperatures are sorely needed, as we explore in the next section.

3.3.5. Deep Thermal Contrasts

Breaking the degeneracy between deep temperature and ammonia contrasts via remote sensing alone (e.g., microwave and infrared) remains a challenge. However, we can gain insights on the likelihood of deep temperature gradients (and winds that increase in speed from the cloud tops to the 5–10-bar level) by (a) considering the stability of the zonal wind solutions, and (b) exploring the results of deep convection models.

For the former, the top-down constraint on the jet structure offered by vorticity measurements support the suggestion that the winds must increase with depth from the cloud-tops to regions near the water cloud (Dowling, 1995). As the meridional gradient of the potential vorticity changes sign at multiple locations (e.g., Read et al., 2006), the cloud-top winds (and our inferred winds at depth) have multiple critical latitudes which could be stable, unstable, or neutrally stable (Dowling, 1995, 2020). Before the descent of the Galileo probe, Dowling (1995) used Voyager-era vorticity measurements (Limaye, 1986) and a shear-stability analysis to determine Jupiter's deep wind profile in the 5–8 bar region. To make the cloud-top critical latitudes stable, rather than marginally stable, required an increase in the amplitude of the underlying eastward jets compared to the cloud-top jets by a factor of ~ 2 , with larger changes at lower latitudes than at midlatitudes. The magnitude of the change depended on the first-baroclinic deformation length, L_d , which remains rather uncertain at depth. Their suggested negative vertical shear of the zonal winds between the tropopause and the 5–8 bar level was later shown to be consistent with Galileo probe results (Atkinson et al., 1998), and qualitatively supports our suggestion that winds strengthen between the cloud-tops and the jovicline in the upper cell (i.e., that kinetic temperatures must vary with latitude, helping to explain the negative pseudoshear in shallow-sounding MWR channels 4–6).

Finally, deep-shell models of turbulent convection in rapidly rotating fluid planets produce nested cylindrical flows aligned with the rotation axis, with alternating zonal jet structures and associated meridional temperature contrasts (Aurnou et al., 2008; Heimpel et al., 2016). These models produce axial thermal plumes parallel to the rotation axis, with the jets acting as barriers to cylindrically radial heat transfer. With warm fluid on the equatorward sides of jets, and cool fluid on the poleward side, the model of Aurnou et al. (2008) exhibits a pattern qualitatively similar to our deep circulation cells ($p > 10$ bars) and opposite to those above the jovicline ($p < 10$ bars). The axial wind structures appropriate for the deeper layers still needs to be properly connected to the radial wind structures in the shallow layers observed by MWR, but this is a compelling

connection suggesting that deep kinetic temperature perturbations (and associated windshear) cannot be ruled out as contributing to the MWR contrasts in the 1–100 bar region.

4. Discussion

Juno MWR observations between August 2016 and April 2018 have revealed that midlatitude gradients in microwave brightness (Δ) are well correlated with the locations of the cloud-top zonal winds, and that this correlation shifts from being negative in shallow-sounding channels (4–6, $\sim p < 5$ bars) to positive in deep-sounding channels (1–3, $\sim p > 5$ bars). As a consequence, cyclonic belts that appear microwave-bright at shallow pressures (i.e., depleted in volatiles and/or physically warm) become microwave dark at higher pressures in the deep atmosphere (i.e., enriched in volatiles and/or physically cool). Using the dependence of Δ_μ on emission angle, and a model-dependent estimate of the MWR contribution functions for each wavelength and viewing geometry, we find that this transition pressure varies considerably with latitude, but is typically found in the 5–10 bar region. The transition is clearest in the southern hemisphere where correlation coefficients are larger, but is also visible in the northern hemisphere. The transition is easier to discern for the broad retrograde jets than the narrow prograde jets, but this may be a consequence of the spatial resolution of MWR failing to capture gradients over narrow (i.e., 1°) latitude ranges.

The belts and zones therefore change their character as a function of depth, irrespective of how the microwave spectra are interpreted (e.g., as compositional variations, temperature variations, or a combination of both). This had been previously noted by Ingersoll et al. (2017) based solely on the PJ1 (August 2016) observations, but they had suggested that the relationship between temperate brightness gradients and the zonal jets was rather poor. Using these same PJ1 data, Duer et al. (2020) also showed the correlation between winds and MWR brightness observations. Using data from subsequent peri-joves, filtering via the deconvolution process of Oyafuso et al. (2020), and by taking the gradient Δ , we have shown that the correlation with the cloud-top winds is actually much better than originally thought.

We now explore the potential consequences of this transition, which we call the “jovicline” via analogy to the thermocline in Earth’s oceans (the transition layer between warm waters near the surface and cool waters at depth) or the tachocline in the Sun’s interior (the transition layer between the interior radiative zone and upper convective zone). However, whereas the terrestrial thermocline is a region with a sharp change in vertical temperature gradient, and resulting change from low-density surface waters to high-density deep waters (the pycnocline), the jovicline is a transitional level where Jupiter’s belt-zone contrasts, and hence the vertical shears, appear to change sign. The jovicline is not to be confused with Jupiter’s “planetary tachocline” at much higher pressures, where Ohmic dissipation on the flows becomes important (Heimpel & Gómez Pérez, 2011). To our knowledge, the first use of the word “thermocline” in a description of Jupiter’s atmosphere appeared in Arthur C. Clarke’s science fiction story, “A Meeting With Medusa,” during the voyage of the *Kon Tiki* balloon down into the cloud layers of Jupiter (Clarke, 1972). Earth’s oceanographic “clines” serve as a barrier to vertical mixing, separating the circulations of the shallow and deep layers. *Might it be possible for the jovicline to act as a similar barrier?*

4.1. Stacked Meridional Circulation Cells

As described in Section 1, the concept of multiple tiers of stacked circulation cells (Fletcher et al., 2020; Ingersoll et al., 2000; Showman & de Pater, 2005) has been used as a possible resolution to the discrepancy between (a) zone-to-belt transport and subsidence in belts above the clouds inferred from Jupiter’s upper tropospheric temperatures and composition, and (b) belt-to-zone transport in Ferrel-like cells below the clouds and upwelling in belts inferred from the prevalence of lightning in Jupiter’s belts (Ingersoll et al., 2000) and the meridional flow required to balance the eddy-momentum flux convergence on the prograde jets (Figure 12a). The change in the microwave brightness contrast across the transition would be consistent with NH_3 (and potentially other gaseous species) being locally depleted in belts in the upper tier, and locally enhanced in belts in the deeper tier (Ingersoll et al., 2017; Showman & de Pater, 2005). The transition between these tiers was assumed to exist somewhere within the cloud-forming region (Showman & de Pater, 2005), where vertical currents would meet and diverge (e.g., Fletcher et al., 2020, assumed it to be near the top-most condensate clouds). Furthermore, numerical simulations of giant planet tropospheres,

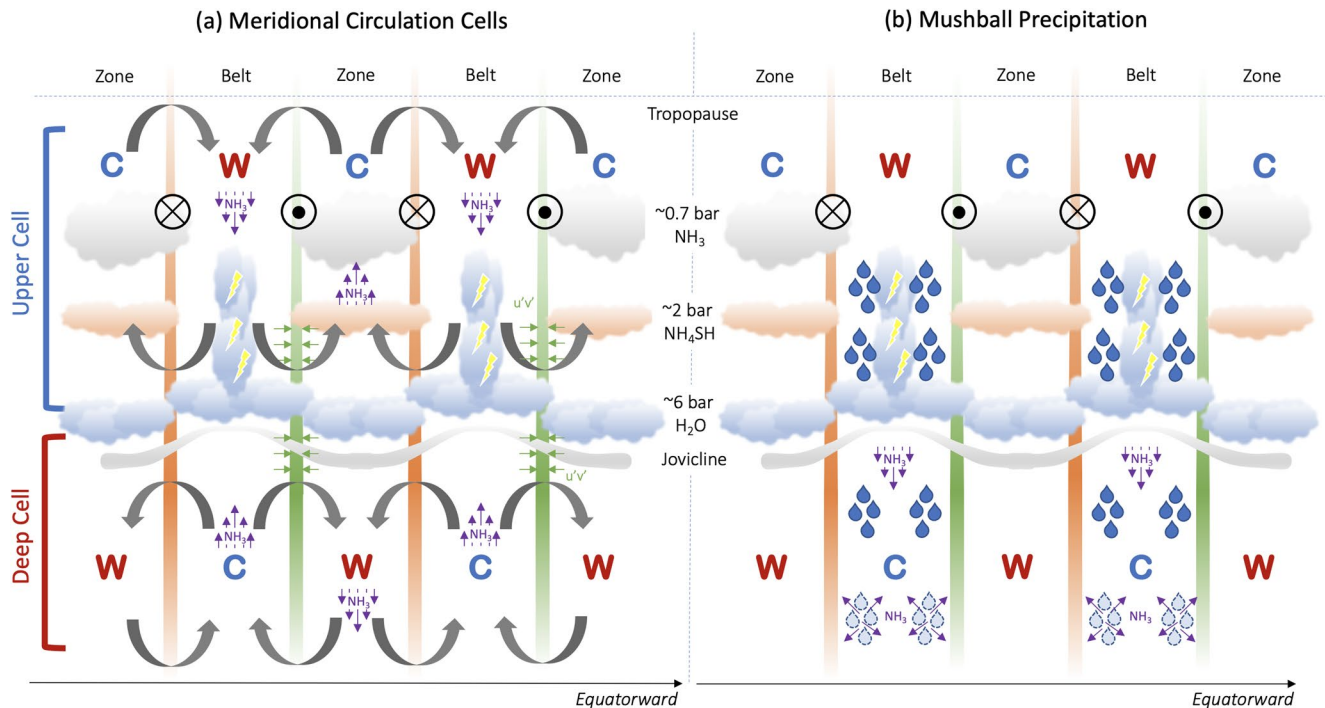


Figure 12. Conceptual diagrams of (a) the stacked system of meridional cells (adapted from Fletcher et al., 2020; Showman & de Pater, 2005), and (b) mushball precipitation (Guillot, Li, et al., 2020). We stress that reality is likely to combine both of these concepts, and all altitudes are qualitative. In both diagrams, high microwave brightness is denoted by a red “W” (warm), low microwave brightness is denoted by a blue “C” (cool); storm plumes are indicated as rising clouds with lightning flashes. The equator is to the right, such that belts have prograde jets on their equatorward edges. Eastward prograde jets are green (with a circular dot indicating motion out of the page) with eddy-momentum flux convergence (small green arrows); westward retrograde jets are orange (with a circular cross indicating motion into the page). The coloration of the green and orange bars indicate wind strengthening through the upper cell and wind decay with depth in the deep cell (“dry convective layer”). The jovicline is shown in gray, co-located with the stable stratification of the water cloud. Purple arrows indicate general ammonia depletion or enrichment, either as a consequence of meridional circulation (gray curved arrows, left) or as a consequence of sequestration in “mushballs,” precipitation, and re-evaporation at great depth (droplets, right), leading to steep vertical NH_3 gradients in the belts.

and particularly the Ferrel-like circulations away from the equator (Spiga et al., 2020; Yamazaki et al., 2005; Young et al., 2018), do appear to support changes in meridional circulation as a function of height, possibly associated with a shift from eddy-forcing of zonal jets within the clouds (Lian & Showman, 2008; Liu & Schneider, 2010; Showman et al., 2006) to a domain of eddy dissipation and wind decay in the upper troposphere.

However, this study suggests that whilst a transition does exist, its likely location is deeper, at or below the water cloud as depicted in the cartoon in Figure 12. Equilibrium cloud condensation models (Atreya et al., 1999) predict that Jupiter’s primary volatiles (NH_3 , H_2S and H_2O) will form cloud decks in the 0.7-to-7-bar range. Specifically, in the absence of microphysical processes and precipitation, solar enrichment of Jupiter’s elemental abundances would place the base of the water cloud near 5.7 bars, whereas a $3\times$ solar enrichment would place it nearer 7.2 bars (Atreya et al., 1999). Given that Jupiter’s tropospheric composition is spatially variable (Achterberg et al., 2006; de Pater et al., 2016; Fletcher et al., 2016; Gierasch et al., 1986; C. Li, Ingersoll, et al., 2017), and that the $T(p)$ and lapse rate may differ between belts and zones, it is reasonable to assume that the water cloud base rises and falls (in the 5–8 bar range) depending on the properties of the atmospheric band. Figure 9a does imply that the transition varies with height on the scale of the belts and zones.

The co-location of the predicted water cloud base with the jovicline may be no coincidence, in that this signifies the transition zone between the dissipative upper layer and the Ferrel-like circulations of the deeper troposphere. The formation of the water cloud produces a density stratification (C. Li & Ingersoll, 2015; Sugiyama et al., 2014; Thomson & McIntyre, 2016), whereby increased molecular weight of the water produces a stabilizing layer that may serve to segregate the deeper circulations in the dry adiabatic layer from those of

the moist upper cells. This stable inversion layer can actually inhibit moist convection until potential energy has accumulated to some critical level, leading to the episodic convective outbursts that appear common within Jupiter's belts (de Pater, Sault, Moeckel, et al., 2019; Fletcher, Orton, et al., 2017; Sánchez-Lavega et al., 2008, 2017; Wong et al., 2020), maybe as part of a “charge-recharge” cycle of CAPE based on water. Note that the upper tier above the water condensation altitude is sometimes referred to as the “weather layer”, but given recent suggestions that NH_3 contrasts extend very deep (Bolton et al., 2017; C. Li, Ingersoll, et al., 2017), we refrain from using this terminology.

In the stacked-cell hypothesis in Figure 12a, belts in the upper cell would be regions of large-scale subsidence creating warm temperatures (and therefore an absence of condensed clouds), zonal wind strengthening with depth (Pirraglia et al., 1981), local ammonia depletion, and therefore a high microwave brightness as we see in the MWR observations for $p < 5$ bar. Conversely, belts in the deeper Ferrel-like cells would be regions of upwelling, with local ammonia enrichment and cooling in regions of adiabatic expansion (and therefore zonal wind decay with depth), leading to the microwave-dark belts that we see in the MWR observations for $p > 10$ bar. Note that this discussion assumes an NH_3 abundance that *decreases* with height throughout both upper and lower tiers, counter to the weak and currently unexplained *increase* of NH_3 with height suggested by MWR inversions in the 2–6 bar region (C. Li, Ingersoll, et al., 2017). As explored in Section 3.3, the observed temperature and/or composition gradients could imply zonal winds increasing in strength from the tropopause to the jovicline, then decaying away slowly with increasing pressure into the dry adiabatic layers, although the strength of the windshear depends on whether temperature or abundance variations are responsible for the observed microwave brightness contrasts. The observed cloud-top winds could therefore be an underestimate of the maximum windspeeds in the upper troposphere (Figure 10b).

However, this contrived picture is incomplete—it does not explain the extreme ammonia enrichment at the equator, nor does it explain why the global-scale NH_3 depletion appears to extend to the 40–60 bar level (Ingersoll et al., 2017; C. Li, Ingersoll, et al., 2017), far deeper than simple precipitation might suggest (e.g., via the inclusion of ammonia rain, C. Li & Chen, 2019). Ferrel-like circulation cells below the jovicline (Showman & de Pater, 2005; Young et al., 2018), balancing eddy-momentum flux convergence on the prograde jets (Salyk et al., 2006), could extend deep even if the forcing is shallow (Lian & Showman, 2008), driving temperature and compositional variability at tens of bars. The belt/zone meridional circulations inferred here may be superimposed onto this larger-scale structure (equatorial NH_3 enrichment, midlatitude NH_3 depletion) driven by precipitation, to be explored in the next section. Lightning could still be prevalent in the belts in Figure 12a with this deeper jovicline, if rising motion from the deep “dry-convecting” layer provides the initial instability to initiate buoyant moist convection and lightning in the water-cloud layers and above (Dowling & Ingersoll, 1989; Thomson & McIntyre, 2016). This could work if the stably stratified transition zone were thinner (and easier to overcome) in the belts compared to the zones—a possible consequence of winds that decay with depth into the deeper layers (Thomson & McIntyre, 2016).

4.2. Precipitation and Microwave Brightness

The complexity of the stacked-cells hypothesis may yet be its undoing, so we should ask *whether vertical and meridional motions are truly required to explain the transition in the microwave belt/zone contrasts*. Recent work by Guillot, Stevenson, et al. (2020) suggested that partially melted hailstones of ammonia dissolved in water ice (nicknamed “mushballs”) could form at 1–2 bar when water is lofted upwards during powerful storms (this is also the level of shallow lightning flashes recently discovered by Juno, Becker et al., 2020). These mushballs then fall deep below the expected water cloud (Figure 12b), to 5–30 bar depending on their properties and the available water ice, where they evaporate, causing cold and volatile-rich evaporative downdrafts that further deplete the condensates. Guillot, Stevenson, et al. (2020) use this process to explain the observed deep depletion of NH_3 down to the 20–30 bar region (Ingersoll et al., 2017; C. Li, Ingersoll, et al., 2017).

As storms are more prevalent within Jupiter's belts, we might expect NH_3 depletion in the upper troposphere to be strongest here (producing the microwave-bright belts for $p < 5$ bars). Similarly, as the mushballs evaporate to relinquish their ammonia (and water), they increase the mean molecular weight in the deeper troposphere, and generate cool downdrafts (Sugiyama et al., 2014). This could lead to a localized NH_3 enhancement in the belts at depth (i.e., microwave-dark belts at $p > 10$ bars). Combined, this leads to

a steep dq_{NH_3} / dz gradient in the belts, shown in Figure 12b, as precipitation dominates over any upward mixing. Conversely, Guillot, Li, et al. (2020) suggested that the absence of storms and mushballs in the Equatorial Zone was responsible for the vertical homogeneity of the NH_3 distribution there. Here we suggest that a shallow dq_{NH_3} / dz gradient could also persist in the extratropical zones for the same reason (i.e., upward mixing dominates over precipitation), providing the contrast to the larger dq_{NH_3} / dz in the stormy belts. At high pressures, slow horizontal mixing would serve to transport NH_3 from belts into zones, and vice versa at lower pressures.

Guillot, Li, et al. (2020) parameterized the storm frequency using the MWR observations of Brown et al. (2018)—however, the detection of lightning sferics in the microwave still placed non-negligible storm flashes in regions considered as zones, and an imperfect relationship between local maxima in the storm rates and the location of the belts. For this reason, the model of Guillot, Li, et al. (2020) (their Figure 6) does not show the banded structure in the temperate domain that is observed in our study. However, if the storm frequency were simply parameterized as being high in the belts and negligible in the zones, we might expect to recover the banding in Figure 1 from this mushball model. In this scenario, the jovicline (and the base of the expected water cloud) is simply the level at which the abundances of NH_3 in the belts and zone are approximately equivalent (Figure 12b), leading to $\Delta = 0$ m/s/km.

As with the stacked-cells hypothesis, the mushball hypothesis remains incomplete. We still need some form of vertical/meridional circulation in the upper troposphere to explain the observed temperatures and distribution of disequilibrium species (e.g., PH_3 enhanced over zones and depleted over belts, and vice versa for para- H_2), and in the deeper troposphere to balance the eddy-momentum flux convergence into the prograde jets (e.g., see review by Fletcher et al., 2020). Given the density stratification contrasts associated with belt/zone differences in mushball formation and evaporation, we might expect some degree of secondary circulation and slow mixing that changes character with depth. So it is possible that the observed transition in belt/zone properties can be explained by a combination of meridional Ferrel-like circulation and mushball precipitation, blending together the processes in Figure 12. Distinguishing between these scenarios may have to wait for more comprehensive GCMs that include the mushball process, and we await such models with great interest.

5. Conclusion

Jupiter's temperate midlatitudes ($\sim \pm 20 - 60^\circ$ latitude) exhibit a banded structure in microwave brightness, characterized by the gradient Δ that is well correlated with the observed latitudes of the cloud-top zonal winds. However, this correlation changes sign between Juno's shallow-sounding channels ($p \sim 0.6 - 5$ bar, $\lambda = 1.4 - 5.75$ cm) and deep-sounding channels ($p \sim 6 - 100$ bars, $\lambda = 11.5 - 50$ cm), implying that Jupiter's belts and zones change their character as a function of depth (Figure 12). The identification of the transition is based on the MWR data alone, independent of radiative transfer and degenerate spectral inversions, but assigning a depth requires model-dependent calculations of microwave contribution functions as a function of emission angle. Based on those calculations, we find that the transition between these two regimes (the "jovicline") appears to separate the layer above the water-condensation region (at 5–8 bars) from the deeper dry adiabatic troposphere. The co-location of this transition with the base of the putative water cloud may be no coincidence, as the molecular weight gradient may have a stabilizing influence, separating two regimes.

If we interpret Δ_μ as being a true reflection of the vertical wind shear (either weak shear associated with compositional gradients, or stronger shear associated with kinetic temperature gradients), then the gradients imply winds that strengthen from the cloud-tops to the jovicline, and then weaken at higher pressures. This is qualitatively consistent with in situ winds measured by Galileo and with winds inferred from shear instability analyses, but we caution that (a) tropical contrasts are likely primarily related to ammonia (C. Li, Ingersoll, et al., 2017), and (b) the strong hemispheric asymmetry between the retrograde SEBs and prograde NTBs jets (e.g., Duer et al., 2020; Kaspi et al., 2018) must be maintained to match Juno's gravity measurements (Figure 10), such that the observed microwave contrasts at low latitudes cannot be solely driven by kinetic temperatures. But at temperate latitudes polewards of $\pm 25^\circ$, the location and direction of the extratropical jets have a smaller influence on the measured gravity field (Galanti et al., 2021), such that

small wind variations with depth at midlatitudes cannot be ruled out. These results hint at the baroclinic nature of Jupiter's atmosphere both above and below the jovicline, but that the jovicline itself may be a region where horizontal temperatures and ammonia distribution are more uniform (leading to a barotropic region where shear tends to zero and winds are more uniform with height).

Using the signatures of gravity waves in the Doppler residuals from the Galileo probe, Allison and Atkinson (2001) explored the evidence for an increase in the static stability below the 5-bar level, suggesting a statically stable layer that they call the "thermocline." This was supported by the idea that large-scale oscillations in thermal emission in the upper troposphere could be due to Rossby waves leaking out of a deeper waveguide (Allison, 1990; Ortiz et al., 1998), and the inferences of a deep stable layer from the propagation of wavefronts from the Shoemaker-Levy 9 impact (Ingersoll et al., 1994). Statically stable layers were also detected in data from the Galileo Probe Atmospheric Structure Investigation at 8 and 14 bar in the probe entry site (Magalhães et al., 2002; Seiff et al., 1998), coinciding with compositional gradients measured by the Galileo Probe Mass Spectrometer (Wong, 2009; Wong et al., 2004). This inferred deep stable layer could be related to the molecular static stability in the water cloud layer, stabilizing the jovicline region.

We explored potential explanations for why the microwave gradients flip sign above and below the jovicline. Maybe stacked tiers of meridional circulation cells (Fletcher et al., 2020; Ingersoll et al., 2000; Showman & de Pater, 2005) are the culprit, with belts exhibiting subsidence (NH_3 depletion and warming) above the jovicline and upwelling (NH_3 enhancement and local cooling) at higher pressures. The Ferrel-like circulation of the deeper cell may be easier to explain because the eddy-momentum flux convergence has been observed (Salyk et al., 2006) and modeled (Young et al., 2018). Conversely, the circulation of the upper cell (where winds decay with altitude through the cloud layers) remains hard to explain because no drag force has yet been adequately identified, although the breaking of vertically propagating waves remains a possible dissipation source (Gierasch et al., 1986; Orsolini & Leovy, 1993; Pirraglia, 1989). Maybe the latitudinal dependence of storms and precipitation, particularly in the properties of "mushballs" (Guillot, Stevenson, et al., 2020), means that the vertical NH_3 gradient is steeper in the belts (lots of storms and associated precipitates) and shallower the zones (less precipitation), which can contribute to the change in character above and below the jovicline. Maybe both of these processes are at work and intricately intertwined.

Irrespective of the interpretation, Juno's MWR has revealed that a significant transition in the microwave brightness of Jupiter's midlatitude belts and zones (associated with ammonia, temperature, or both) occurs in the 5–10 bar region, and we hope that future studies will allow us to explain its origins.

Acknowledgments

Fletcher is a Juno Participating Scientist supported by a Royal Society Research Fellowship and European Research Council Consolidator Grant (under the European Union's Horizon 2020 research and innovation programme, grant agreement no 723890) at the University of Leicester. Orton is supported by funds from NASA distributed to the Jet Propulsion Laboratory, California Institute of Technology. Some of this research was carried out at the Jet Propulsion Laboratory, California Institute of Technology, under a contract with the National Aeronautics and Space Administration (80NM0018D0004). Wong is supported by NASA's Juno Participating Scientist program through grant 80NSSC19K1265 to SETI Institute. Kaspi, Galanti, and Duer are supported by the Minerva Foundation and the Helen Kimmel Center for Planetary Science at the Weizmann Institute of Science. Guillot is supported by a grant from the Centre National d'Etudes Spatiales. The authors are grateful to J. Rogers for helpful insights into features in Jupiter's STB and NTB, T. Dowling and J. Aurnou for insights on deep temperature gradients, and to two anonymous reviewers for helping to improve the quality of this article.

Data Availability Statement

Juno observations are available through the Planetary Data System Atmospheres Node (https://pds-atmospheres.nmsu.edu/data_and_services/atmospheres_data/JUNO/microwave.html), and links to the specific calibrated MWR data (https://pds-atmospheres.nmsu.edu/PDS/data/jnomwr_1100/). Data for individual figures are available through Zenodo (<https://doi.org/10.5281/zenodo.4761404>).

References

- Achterberg, R. K., Conrath, B. J., & Gierasch, P. J. (2006). Cassini CIRS retrievals of ammonia in Jupiter's upper troposphere. *Icarus*, 182, 169–180. <https://doi.org/10.1016/j.icarus.2005.12.020>
- Allison, M. (1990). Planetary waves in Jupiter's equatorial atmosphere. *Icarus*, 83, 282–307. [https://doi.org/10.1016/0019-1035\(90\)90069-L](https://doi.org/10.1016/0019-1035(90)90069-L)
- Allison, M., & Atkinson, D. H. (2001). Galileo Probe Doppler residuals as the wave-dynamical signature of weakly stable, downward-increasing stratification in Jupiter's deep wind layer. *Geophysical Research Letters*, 28, 2747–2750. <https://doi.org/10.1029/2001GL012927>
- Antuñano, A., Fletcher, L. N., Orton, G. S., Melin, H., Milan, S., Rogers, J., et al. (2019). Jupiter's atmospheric variability from long-term ground-based observations at 5 μm . *Astronomical Journal*, 158(3), 130. <https://doi.org/10.3847/1538-3881/ab2cd6>
- Atkinson, D. H. (2001). The Galileo Jupiter Probe Doppler wind experiment. *Solar System Research*, 35(5), 354–375. <https://doi.org/10.1023/a:1012348103693>
- Atkinson, D. H., Pollack, J. B., & Seiff, A. (1998). The Galileo probe Doppler wind experiment: Measurement of the deep zonal winds on Jupiter. *Journal of Geophysical Research*, 103, 22911–22928. <https://doi.org/10.1029/98JE00060>
- Atreya, S. K., Wong, M. H., Owen, T. C., Mahaffy, P. R., Niemann, H. B., de Pater, I., et al. (1999). A comparison of the atmospheres of Jupiter and Saturn: Deep atmospheric composition, cloud structure, vertical mixing, and origin. *Planetary and Space Science*, 47, 1243–1262. [https://doi.org/10.1016/s0032-0633\(99\)00047-1](https://doi.org/10.1016/s0032-0633(99)00047-1)
- Aurnou, J., Heimpel, M., Allen, L., King, E., & Wicht, J. (2008). Convective heat transfer and the pattern of thermal emission on the gas giants. *Geophysical Journal International*, 173(3), 793–801. <https://doi.org/10.1111/j.1365-246X.2008.03764.x>

- Baines, K. H., Simon-Miller, A. A., Orton, G. S., Weaver, H. A., Lunsford, A., Momary, T. W., et al. (2007). Polar lightning and decadal-scale cloud variability on Jupiter. *Science*, 318, 226–229. <https://doi.org/10.1126/science.1147912>
- Becker, H. N., Alexander, J. W., Atreya, S. K., Bolton, S. J., Brennan, M. J., Brown, S. T., et al. (2020). Small lightning flashes from shallow electrical storms on Jupiter. *Nature*, 584(7819), 55–58. <https://doi.org/10.1038/s41586-020-2532-1>
- Bellotti, A., Steffes, P. G., & Chinsomboon, G. (2016). Laboratory measurements of the 5–20 cm wavelength opacity of ammonia, water vapor, and methane under simulated conditions for the deep jovian atmosphere. *Icarus*, 280, 255–267. <https://doi.org/10.1016/j.icarus.2016.07.013>
- Bolton, S. J., Adriani, A., Adumitroaie, V., Allison, M., Anderson, J., Atreya, S., et al. (2017). Jupiter's interior and deep atmosphere: The initial pole-to-pole passes with the Juno spacecraft. *Science*, 356, 821–825. <https://doi.org/10.1126/science.aal2108>
- Brown, S., Janssen, M., Adumitroaie, V., Atreya, S., Bolton, S., Gulkis, S., et al. (2018). Prevalent lightning sferics at 600 megahertz near Jupiter's poles. *Nature*, 558, 87–90. <https://doi.org/10.1038/s41586-018-0156-5>
- Buccino, D. R., Helled, R., Parisi, M., Hubbard, W. B., & Folkner, W. M. (2020). Updated equipotential shapes of Jupiter and Saturn using Juno and Cassini grand finale gravity science measurements. *Journal of Geophysical Research: Planets*, 125(8), e06354. <https://doi.org/10.1029/2019JE006354>
- Cao, H., & Stevenson, D. J. (2017). Zonal flow magnetic field interaction in the semi-conducting region of giant planets. *Icarus*, 296, 59–72. <https://doi.org/10.1016/j.icarus.2017.05.015>
- Clarke, A. C. (1972). *The wind from the sun*. Harcourt Brace Jovanovich, Inc.
- Conrath, B. J., Gierasch, P. J., & Leroy, S. S. (1990). Temperature and circulation in the stratosphere of the outer planets. *Icarus*, 83, 255–281. [https://doi.org/10.1016/0019-1035\(90\)90068-K](https://doi.org/10.1016/0019-1035(90)90068-K)
- Conrath, B. J., Gierasch, P. J., & Ustinov, E. A. (1998). Thermal structure and para hydrogen fraction on the outer planets from Voyager IRIS measurements. *Icarus*, 135, 501–517. <https://doi.org/10.1006/icar.1998.6000>
- Conrath, B. J., & Pirraglia, J. A. (1983). Thermal structure of Saturn from Voyager infrared measurements—Implications for atmospheric dynamics. *Icarus*, 53, 286–292. [https://doi.org/10.1016/0019-1035\(83\)90148-3](https://doi.org/10.1016/0019-1035(83)90148-3)
- de Pater, I., Sault, R. J., Butler, B., DeBoer, D., & Wong, M. H. (2016). Peering through Jupiter's clouds with radio spectral imaging. *Science*, 352, 1198–1201. <https://doi.org/10.1126/science.aaf2210>
- de Pater, I., Sault, R. J., Moeckel, C., Moullet, A., Wong, M. H., Goullaud, C., et al. (2019). First ALMA millimeter-wavelength maps of Jupiter, with a multiwavelength study of convection. *Astronomical Journal*, 158(4), 139. <https://doi.org/10.3847/1538-3881/ab3643>
- de Pater, I., Sault, R. J., Wong, M. H., Fletcher, L. N., DeBoer, D., & Butler, B. (2019). Jupiter's ammonia distribution derived from VLA maps at 3–37 GHz. *Icarus*, 322, 168–191. <https://doi.org/10.1016/j.icarus.2018.11.024>
- Dowling, T. E. (1995). Estimate of Jupiter's deep zonal-wind profile from Shoemaker-Levy 9 data and Arnold's second stability criterion. *Icarus*, 117, 439–442. <https://doi.org/10.1006/icar.1995.1169>
- Dowling, T. E. (2020). Jupiter-style jet stability. *The Planetary Science Journal*, 1(1), 6. <https://doi.org/10.3847/PSJ/ab789d>
- Dowling, T. E., & Ingersoll, A. P. (1989). Jupiter's Great Red Spot as a shallow water system. *Journal of the Atmospheric Sciences*, 46, 3256–3278. [https://doi.org/10.1175/1520-0469\(1989\)046<3256:JGRSAA>2.0.CO;2](https://doi.org/10.1175/1520-0469(1989)046<3256:JGRSAA>2.0.CO;2)
- Duer, K., Galanti, E., & Kaspi, Y. (2020). The range of Jupiter's flow structures that fit the Juno asymmetric gravity measurements. *Journal of Geophysical Research: Planets*, 125(8), e06292. <https://doi.org/10.1029/2019JE006292>
- Flasar, F. M. (1986). Global dynamics and thermal structure of Jupiter's atmosphere. *Icarus*, 65(2–3), 280–303. [https://doi.org/10.1016/0019-1035\(86\)90140-5](https://doi.org/10.1016/0019-1035(86)90140-5)
- Fletcher, L. N., de Pater, I., Reach, W. T., Wong, M., Orton, G. S., Irwin, P. G. J., & Gehrz, R. D. (2017). Jupiter's para-H₂ distribution from SOFIA/FORCAST and Voyager/IRIS 17–37 μ m spectroscopy. *Icarus*, 286, 223–240. <https://doi.org/10.1016/j.icarus.2016.10.002>
- Fletcher, L. N., Greathouse, T. K., Orton, G. S., Sinclair, J. A., Giles, R. S., Irwin, P. G. J., & Encenaz, T. (2016). Mid-infrared mapping of Jupiter's temperatures, aerosol opacity and chemical distributions with IRTF/TEXES. *Icarus*, 278, 128–161. <https://doi.org/10.1016/j.icarus.2016.06.008>
- Fletcher, L. N., Kaspi, Y., Guillot, T., & Showman, A. P. (2020). How well do we understand the belt/zone circulation of giant planet atmospheres? *Space Science Reviews*, 216(2), 30. <https://doi.org/10.1007/s11214-019-0631-9>
- Fletcher, L. N., Orton, G. S., Rogers, J. H., Giles, R. S., Payne, A. V., Irwin, P. G. J., & Viedovato, M. (2017). Moist convection and the 2010–2011 revival of Jupiter's South Equatorial Belt. *Icarus*, 286, 94–117. <https://doi.org/10.1016/j.icarus.2017.01.001>
- Fletcher, L. N., Orton, G. S., Teanby, N. A., & Irwin, P. G. J. (2009). Phosphine on Jupiter and Saturn from Cassini/CIRS. *Icarus*, 202, 543–564. <https://doi.org/10.1016/j.icarus.2009.03.023>
- Galanti, E., & Kaspi, Y. (2021). Combined magnetic and gravity measurements probe the deep zonal flows of the gas giants. *Monthly Notices of the Royal Astronomical Society*, 501(2), 2352–2362. <https://doi.org/10.1093/mnras/staa3722>
- Galanti, E., Kaspi, Y., Duer, K., Fletcher, L., Ingersoll, A. P., Li, C., et al. (2021). Constraints on the latitudinal profile of Jupiter's deep jets. *Geophysical Research Letters*, 48, e2021GL092912. <https://doi.org/10.1029/2021GL092912>
- Gierasch, P. J., Ingersoll, A. P., Banfield, D., Ewald, S. P., Helfenstein, P., Simon-Miller, A., et al. (2000). Observation of moist convection in Jupiter's atmosphere. *Nature*, 403, 628–630. <https://doi.org/10.1038/35001017>
- Gierasch, P. J., Magalhaes, J. A., & Conrath, B. J. (1986). Zonal mean properties of Jupiter's upper troposphere from Voyager infrared observations. *Icarus*, 67, 456–483. [https://doi.org/10.1016/0019-1035\(86\)90125-9](https://doi.org/10.1016/0019-1035(86)90125-9)
- Giles, R. S., Fletcher, L. N., & Irwin, P. G. J. (2017). Latitudinal variability in Jupiter's tropospheric disequilibrium species: GeH₄, AsH₃ and PH₃. *Icarus*, 289, 254–269. <https://doi.org/10.1016/j.icarus.2016.10.023>
- Grassi, D., Adriani, A., Mura, A., Atreya, S. K., Fletcher, L. N., Lunine, J. I., et al. (2020). On the spatial distribution of minor species in Jupiter's troposphere as inferred from Juno JIRAM data. *Journal of Geophysical Research: Planets*, 125(4), e06206. <https://doi.org/10.1029/2019JE006206>
- Guillot, T., Li, C., Bolton, S. J., Brown, S. T., Ingersoll, A. P., Janssen, M. A., et al. (2020). Storms and the depletion of ammonia in Jupiter: II. Explaining the Juno observations. *Journal of Geophysical Research: Planets*, 125(8), e06404. <https://doi.org/10.1029/2020JE006404>
- Guillot, T., Miguel, Y., Militzer, B., Hubbard, W. B., Kaspi, Y., Galanti, E., et al. (2018). A suppression of differential rotation in Jupiter's deep interior. *Nature*, 555, 227–230. <https://doi.org/10.1038/nature25775>
- Guillot, T., Stevenson, D. J., Atreya, S. K., Bolton, S. J., & Becker, H. N. (2020). Storms and the depletion of ammonia in Jupiter: I. Microphysics of “mushballs”. *Journal of Geophysical Research: Planets*, 125(8), e06403. <https://doi.org/10.1029/2020JE006403>
- Hanley, T. R., Steffes, P. G., & Karpowicz, B. M. (2009). A new model of the hydrogen and helium-broadened microwave opacity of ammonia based on extensive laboratory measurements. *Icarus*, 202, 316–335. <https://doi.org/10.1016/j.icarus.2009.02.002>
- Heimpel, M., Gastine, T., & Wicht, J. (2016). Simulation of deep-seated zonal jets and shallow vortices in gas giant atmospheres. *Nature Geoscience*, 9(1), 19–23. <https://doi.org/10.1038/ngeo2601>

- Heimpel, M., & Gómez Pérez, N. (2011). On the relationship between zonal jets and dynamo action in giant planets. *Geophysical Research Letters*, 38(14), L14201. <https://doi.org/10.1029/2011GL047562>
- Hess, S. L., & Panofsky, H. A. (1951). The atmospheres of the other planets. In T. F. Malone (Ed.), *Compendium of meteorology* (pp. 391–398). American Meteorological Society. https://doi.org/10.1007/978-1-940033-70-9_34
- Hockey, T. (1999). *Galileo's planet: Observing Jupiter before photography*. Institute of Physics Publishing.
- Holton, J. (2004). *An introduction to dynamic meteorology*. Academic Press.
- Ingersoll, A. P., Adumitroaie, V., Allison, M. D., Atreya, S., Bellotti, A. A., Bolton, S. J., et al. (2017). Implications of the ammonia distribution on Jupiter from 1 to 100 bars as measured by the Juno microwave radiometer. *Geophysical Research Letters*, 44, 7676–7685. <https://doi.org/10.1002/2017GL074277>
- Ingersoll, A. P., Beebe, R., Mitchell, J., Garneau, G., Yagi, G., & Muller, J. (1981). Interaction of eddies and mean zonal flow on Jupiter as inferred from Voyager 1 and 2 images. *Journal of Geophysical Research*, 86, 8733–8743. <https://doi.org/10.1029/ja086ia10p08733>
- Ingersoll, A. P., Gierasch, P. J., Banfield, D., Vasavada, A. R., & Galileo Imaging Team. (2000). Moist convection as an energy source for the large-scale motions in Jupiter's atmosphere. *Nature*, 403, 630–632. <https://doi.org/10.1038/35001021>
- Ingersoll, A. P., Kanamori, H., & Dowling, T. E. (1994). Atmospheric gravity waves from the impact of comet Shoemaker-Levy 9 with Jupiter. *Geophysical Research Letters*, 21(11), 1083–1086. <https://doi.org/10.1029/94GL01057>
- Iñurrigarro, P., Hueso, R., Legarreta, J., Sánchez-Lavega, A., Eichstädt, G., Rogers, J. H., et al. (2020). Observations and numerical modeling of a convective disturbance in a large-scale cyclone in Jupiter's South Temperate Belt. *Icarus*, 336, 113475. <https://doi.org/10.1016/j.icarus.2019.113475>
- Janssen, M. A., Oswald, J. E., Brown, S. T., Gulkis, S., Levin, S. M., Bolton, S. J., et al. (2017). MWR: Microwave radiometer for the Juno mission to Jupiter. *Space Science Reviews*, 213, 139–185. <https://doi.org/10.1007/s11214-017-0349-5>
- Kaspi, Y., Flierl, G. R., & Showman, A. P. (2009). The deep wind structure of the giant planets: Results from an anelastic general circulation model. *Icarus*, 202(2), 525–542. <https://doi.org/10.1016/j.icarus.2009.03.026>
- Kaspi, Y., Galanti, E., Hubbard, W. B., Stevenson, D. J., Bolton, S. J., Iess, L., et al. (2018). Jupiter's atmospheric jet streams extend thousands of kilometres deep. *Nature*, 555, 223–226. <https://doi.org/10.1038/nature25793>
- Kaspi, Y., Galanti, E., Showman, A. P., Stevenson, D. J., Guillot, T., Iess, L., & Bolton, S. J. (2020). Comparison of the deep atmospheric dynamics of Jupiter and Saturn in light of the Juno and Cassini gravity measurements. *Space Science Reviews*, 216(5), 84. <https://doi.org/10.1007/s11214-020-00705-7>
- Li, C., & Chen, X. (2019). Simulating Nonhydrostatic Atmospheres on Planets (SNAP): Formulation, Validation, and Application to the Jovian Atmosphere. *The Astrophysical Journal Supplement Series*, 240(2), 37. <https://doi.org/10.3847/1538-4365/aafdaa>
- Li, C., Ingersoll, A., Bolton, S., Levin, S., Janssen, M., Atreya, S., et al. (2020). The water abundance in Jupiter's equatorial zone. *Nature Astronomy*, 4, 609–616. <https://doi.org/10.1038/s41550-020-1009-3>
- Li, C., & Ingersoll, A. P. (2015). Moist convection in hydrogen atmospheres and the frequency of Saturn's giant storms. *Nature Geoscience*, 8, 398–403. <https://doi.org/10.1038/ngeo2405>
- Li, C., Ingersoll, A. P., Janssen, M., Levin, S., Bolton, S., Adumitroaie, V., et al. (2017). The distribution of ammonia on Jupiter from a preliminary inversion of Juno microwave radiometer data. *Geophysical Research Letters*, 44, 5317–5325. <https://doi.org/10.1002/2017GL073159>
- Li, C., Oyafuso, F. A., Brown, S. T., Atreya, S. K., Orton, G., Ingersoll, A. P., & Janssen, M. A. (2017). *How deep is Jupiter's Great Red Spot?* AGU Fall Meeting Abstracts.
- Li, L., Ingersoll, A. P., Vasavada, A. R., Simon-Miller, A. A., Achterberg, R. K., Ewald, S. P., et al. (2006). Waves in Jupiter's atmosphere observed by the Cassini ISS and CIRS instruments. *Icarus*, 185, 416–429. <https://doi.org/10.1016/j.icarus.2006.08.005>
- Li, L., Ingersoll, A. P., Vasavada, A. R., Simon-Miller, A. A., Del Genio, A. D., Ewald, S. P., et al. (2006). Vertical wind shear on Jupiter from Cassini images. *Journal of Geophysical Research*, 111, 4004. <https://doi.org/10.1029/2005JE002556>
- Lian, Y., & Showman, A. P. (2008). Deep jets on gas-giant planets. *Icarus*, 194, 597–615. <https://doi.org/10.1016/j.icarus.2007.10.014>
- Limaye, S. S. (1986). Jupiter—New estimates of the mean zonal flow at the cloud level. *Icarus*, 65, 335–352. [https://doi.org/10.1016/0019-1035\(86\)90142-9](https://doi.org/10.1016/0019-1035(86)90142-9)
- Little, B., Anger, C. D., Ingersoll, A. P., Vasavada, A. R., Senske, D. A., Breneman, H. H., et al. (1999). Galileo images of lightning on Jupiter. *Icarus*, 142, 306–323. <https://doi.org/10.1006/icar.1999.6195>
- Liu, J., Goldreich, P. M., & Stevenson, D. J. (2008). Constraints on deep-seated zonal winds inside Jupiter and Saturn. *Icarus*, 196, 653–664. <https://doi.org/10.1016/j.icarus.2007.11.036>
- Liu, J., & Schneider, T. (2010). Mechanisms of jet formation on the giant planets. *Journal of the Atmospheric Sciences*, 67, 3652–3672. <https://doi.org/10.1175/2010JAS3492.1>
- Lunine, J. I., & Hunten, D. M. (1987). Moist convection and the abundance of water in the troposphere of Jupiter. *Icarus*, 69(3), 566–570. [https://doi.org/10.1016/0019-1035\(87\)90025-X](https://doi.org/10.1016/0019-1035(87)90025-X)
- Magalhães, J. A., Seiff, A., & Young, R. E. (2002). The stratification of Jupiter's troposphere at the Galileo probe entry site. *Icarus*, 158, 410–433. <https://doi.org/10.1006/icar.2002.6891>
- Orsolini, Y., & Leovy, C. B. (1993). A model of large-scale instabilities in the Jovian troposphere. 1. Linear model. *Icarus*, 106(2), 392–405. <https://doi.org/10.1006/icar.1993.1180>
- Ortiz, J. L., Orton, G. S., Friedson, A. J., Stewart, S. T., Fisher, B. M., & Spencer, J. R. (1998). Evolution and persistence of 5- μ m hot spots at the Galileo probe entry latitude. *Journal of Geophysical Research*, 103, 23051–23069. <https://doi.org/10.1029/98JE00696>
- Oyafuso, F., Levin, S., Orton, G., Brown, S. T., Adumitroaie, V., Janssen, M., et al. (2020). Angular dependence and spatial distribution of Jupiter's centimeter-wave thermal emission from Juno's microwave radiometer. *Earth and Space Science*, 7(11), e01254. <https://doi.org/10.1029/2020EA001254>
- Pirraglia, J. A. (1989). Dissipationless decay of Jovian jets. *Icarus*, 79, 196–207. [https://doi.org/10.1016/0019-1035\(89\)90116-4](https://doi.org/10.1016/0019-1035(89)90116-4)
- Pirraglia, J. A., Conrath, B. J., Allison, M. D., & Gierasch, P. J. (1981). Thermal structure and dynamics of Saturn and Jupiter. *Nature*, 292(5825), 677–679. <https://doi.org/10.1038/292677a0>
- Porco, C. C., West, R. A., McEwen, A., Del Genio, A. D., Ingersoll, A. P., Thomas, P., et al. (2003). Cassini imaging of Jupiter's atmosphere, satellites, and rings. *Science*, 299, 1541–1547. <https://doi.org/10.1126/science.1079462>
- Read, P., Gierasch, P., Conrath, B., Simon-Miller, A., Fouchet, T., & Yamazaki, Y. (2006). Mapping potential-vorticity dynamics on Jupiter. I: Zonal-mean circulation from Cassini and Voyager 1 data. *Quarterly Journal of the Royal Meteorological Society*, 132, 1577–1603. <https://doi.org/10.1256/qj.05.34>
- Salyk, C., Ingersoll, A., Lorre, J., Vasavada, A., & Del Genio, A. (2006). Interaction between eddies and mean flow in Jupiter's atmosphere: Analysis of Cassini imaging data. *Icarus*, 185(2), 430–442. <https://doi.org/10.1016/j.icarus.2006.08.007>

- Sánchez-Lavega, A., Orton, G. S., Hueso, R., García-Melendo, E., Pérez-Hoyos, S., Simon-Miller, A., et al. (2008). Depth of a strong Jovian jet from a planetary-scale disturbance driven by storms. *Nature*, *451*, 437–440. <https://doi.org/10.1038/nature06533>
- Sánchez-Lavega, A., Rogers, J. H., Orton, G. S., García-Melendo, E., Legarreta, J., Colas, F., et al. (2017). A planetary-scale disturbance in the most intense Jovian atmospheric jet from JunoCam and ground-based observations. *Geophysical Research Letters*, *44*, 4679–4686. <https://doi.org/10.1002/2017GL073421>
- Seiff, A., Kirk, D. B., Knight, T. C. D., Young, R. E., Mihalov, J. D., Young, L. A., et al. (1998). Thermal structure of Jupiter's atmosphere near the edge of a 5- μ m hot spot in the north equatorial belt. *Journal of Geophysical Research*, *103*, 22857–22889. <https://doi.org/10.1029/98JE01766>
- Showman, A. P., & de Pater, I. (2005). Dynamical implications of Jupiter's tropospheric ammonia abundance. *Icarus*, *174*, 192–204. <https://doi.org/10.1016/j.icarus.2004.10.004>
- Showman, A. P., & Dowling, T. E. (2000). Nonlinear simulations of Jupiter's 5-micron hot spots. *Science*, *289*, 1737–1740. <https://doi.org/10.1126/science.289.5485.1737>
- Showman, A. P., Gierasch, P. J., & Lian, Y. (2006). Deep zonal winds can result from shallow driving in a giant-planet atmosphere. *Icarus*, *182*, 513–526. <https://doi.org/10.1016/j.icarus.2006.01.019>
- Simon-Miller, A. A., Conrath, B. J., Gierasch, P. J., Orton, G. S., Achterberg, R. K., Flasar, F. M., & Fisher, B. M. (2006). Jupiter's atmospheric temperatures: From Voyager IRIS to Cassini CIRS. *Icarus*, *180*, 98–112. <https://doi.org/10.1016/j.icarus.2005.07.019>
- Spiga, A., Guerlet, S., Millour, E., Indurain, M., Meurdesoif, Y., Cabanes, S., et al. (2020). Global climate modeling of Saturn's atmosphere. Part II: Multi-annual high-resolution dynamical simulations. *Icarus*, *335*, 113377. <https://doi.org/10.1016/j.icarus.2019.07.011>
- Stone, P. H. (1976). The meteorology of the Jovian atmosphere. In T. Gehrels, & S. Matthews (Eds.), *IAU colloq. 30: Jupiter: Studies of the interior, atmosphere, magnetosphere and satellites* (pp. 586–618).
- Sugiyama, K., Nakajima, K., Odaka, M., Kuramoto, K., & Hayashi, Y.-Y. (2014). Numerical simulations of Jupiter's moist convection layer: Structure and dynamics in statistically steady states. *Icarus*, *229*, 71–91. <https://doi.org/10.1016/j.icarus.2013.10.016>
- Sun, Z.-P., Schubert, G., & Stoker, C. R. (1991). Thermal and humidity winds in outer planet atmospheres. *Icarus*, *91*(1), 154–160. [https://doi.org/10.1016/0019-1035\(91\)90134-F](https://doi.org/10.1016/0019-1035(91)90134-F)
- Thomson, S. I., & McIntyre, M. E. (2016). Jupiter's unearthy jets: A new turbulent model exhibiting statistical steadiness without large-scale dissipation. *Journal of the Atmospheric Sciences*, *73*, 1119–1141. <https://doi.org/10.1175/JAS-D-14-0370.1>
- Tollefson, J., Wong, M. H., de Pater, I., Simon, A. A., Orton, G. S., Rogers, J. H., et al. (2017). Changes in Jupiter's Zonal Wind Profile preceding and during the Juno mission. *Icarus*, *296*, 163–178. <https://doi.org/10.1016/j.icarus.2017.06.007>
- Vallis, G. K. (2006). *Atmospheric and oceanic fluid dynamics*. <https://doi.org/10.2277/0521849691>
- von Zahn, U., Hunten, D. M., & Lehmacher, G. (1998). Helium in Jupiter's atmosphere: Results from the Galileo probe helium interferometer experiment. *Journal of Geophysical Research*, *103*(12), 22815–22829. <https://doi.org/10.1029/98JE00695>
- Weidenschilling, S. J., & Lewis, J. S. (1973). Atmospheric and cloud structures of the Jovian planets. *Icarus*, *20*, 465–476. [https://doi.org/10.1016/0019-1035\(73\)90019-5](https://doi.org/10.1016/0019-1035(73)90019-5)
- West, R., Baines, K., Friedson, A., Banfield, D., Ragent, B., & Taylor, F. (2004). *Jupiter: The planet, satellites and magnetosphere* (pp. 79–104).
- Wong, M. H. (2009). Comment on “Transport of nonmethane hydrocarbons to Jupiter's troposphere by descent of smog particles” by Donald M. Hunten [Icarus 194 (2008) 616–622]. *Icarus*, *199*, 231–235. <https://doi.org/10.1016/j.icarus.2008.08.017>
- Wong, M. H., Mahaffy, P., Atreya, S., Niemann, H., & Owen, T. (2004). Updated Galileo probe mass spectrometer measurements of carbon, oxygen, nitrogen, and sulfur on Jupiter. *Icarus*, *171*(1), 153–170. <https://doi.org/10.1016/j.icarus.2004.04.010>
- Wong, M. H., Simon, A. A., Tollefson, J. W., de Pater, I., Barnett, M. N., Hsu, A. I., et al. (2020). High-resolution UV/Optical/IR Imaging of Jupiter in 2016–2019. *Astrophysical Journal Supplement*, *247*(2), 58. <https://doi.org/10.3847/1538-4365/ab775f>
- Yamazaki, Y. H., Read, P. L., & Skeet, D. R. (2005). Hadley circulations and Kelvin wave-driven equatorial jets in the atmospheres of Jupiter and Saturn. *Planetary and Space Science*, *53*, 508–525. <https://doi.org/10.1016/j.pss.2004.03.009>
- Young, R. M., Read, P. L., & Wang, Y. (2018). Simulating Jupiter's weather layer. Part I: Jet spin-up in a dry atmosphere. *Icarus*. <https://doi.org/10.1016/j.icarus.2018.12.005>
- Zuchowski, L. C., Yamazaki, Y. H., & Read, P. L. (2009). Modeling Jupiter's cloud bands and decks. 1. Jet scale meridional circulations. *Icarus*, *200*, 548–562. <https://doi.org/10.1016/j.icarus.2008.11.024>